FINITE ELEMENT MODEL OF A PIEZO-FILM ACCELEROMETER

A Thesis Submitted

to the College of Graduate Studies and Research

in Partial Fulfillment of the Requirements

for the Degree of Master of Science

in the Department of Electrical Engineering

University of Saskatchewan

Saskatoon

by

Enas Mohamed

PERMISSION TO USE

In presenting this thesis in partial fulfillment of the requirements for a Postgraduate degree from the University of Saskatchewan, it is agreed that the Libraries of this University may make it freely available for inspection. Permission for copying of this thesis in any manner, in whole or in part, for scholarly purposes may be granted by the professors who supervised this thesis work or, in their absence, by the Head of the Department of Electrical Engineering or the Dean of the College of Graduate Studies and Research at the University of Saskatchewan. Any copying, publication, or use of this thesis, or parts thereof, for financial gain without the written permission of the author is strictly prohibited. Proper recognition shall be given to the author and to the University of Saskatchewan in any scholarly use which may be made of any material in this thesis.

Request for permission to copy or to make any other use of material in this thesis in whole or in part should be addressed to:

Head of the Department of Electrical Engineering
57 Campus Drive
University of Saskatchewan
Saskatoon, Saskatchewan, Canada
S7N 5A9

ACKNOWLEDGMENTS

I would like to express my sincere gratitude and appreciation to my supervisor, Dr. Brian Daku for his guidance throughout the course of this work, his encouragement and financial assistance.

The National Science and Engineering Research Council (NSERC) and the Department of Electrical Engineering are also gratefully acknowledged for providing financial support for this research.

I also thank Dr. Bruce Sparling and Greg Del Frari for all the willing discussions pertaining to this research. I also acknowledge all help extended by Daniel Teng, Trevor Zintel and Dave Karaloff.

A special thanks goes out to my parents and family, for their continued love and endless encouragement. For without them, none of this would have been possible.

UNIVERSITY OF SASKATCHEWAN

Electrical Engineering Abstract

FINITE ELEMENT MODEL OF A PIEZO-FILM ACCELEROMETER

Student: Enas Mohamed

Supervisor: Prof. Brian Daku

M.Sc. Thesis Submitted to the

College of Graduate Studies and Research

2004

ABSTRACT

Piezo-film sensors are being increasingly applied in the development of many structures. But in developing these components, it is difficult and costly to rely only on experiments. Fortunately, the availability of computer software as finite element analysis programs, can be used to predict and develop the performance of these devices.

The aim of this research was to develop a finite element model for a unique, low-cost robust acceleration transducer. The accelerometer under study was used for low frequency vibration monitoring, using piezo-film sheets.

The finite element model was developed using the commercial software package, ADINA. The finite element model was validated by comparing the model results to laboratory and theoretical results. The responses for all three approaches were similar for a constant acceleration. In addition, the natural frequency of the system

calculated from the theoretical and numerical results were within the percentage error limit.

The stress on the piezo-film sheets was also studied via the finite element model. It was found to be within the piezo-film yield strength, ensuring no breakage of the piezo-film sheets.

Finally, as this sensor could be used in other applications, the finite element model was utilized to change some of the sensor design parameters and study the effect of these changes with respect to natural frequency of the system to suit other sensor applications.

Table of Contents

List of Figures

List of Tables

List of Abbreviations

2D	2-Dimension
3D	3-Dimension
ADINA	Automatic Dynamic Incremental Nonlinear Analysis
AUI	ADINA User Interface
dB	deciBels
DOF	Degree of Freedom
FE	Finite Element
FEA	Finite Element Analysis
FEM	Finite Element Method
I/P	Input
O/P	Output
PC	Personal Computer
PVDF	Polyvinylidene Fluoride

1. INTRODUCTION

Condition or vibration monitoring is an important issue for mankind's safety. The objective in all condition monitoring systems is to obtain the earliest possible warning of damage or malfunction. In much of conventional industry the advantage of having an 'early warning' system is to allow shutdowns to be scheduled at convenient times. Sometimes the requirement is more critical, as with monitoring seismic activity in mines, adequate warning will help evacuate men and machinery in reasonable time. Generally, vibrational sensors for monitoring micro-seismic activities consist of several geophones. These geophones are mass-spring devices that generate a signal using a magnet and a coil when a micro-seismic event occurs. For proper condition monitoring a large number of geophones has to be installed in the mine and many of these costly geophones cannot be recovered. The present work which involves developing alternative low-cost disposable vibrational sensors addresses this problem. In the development process, new ideas for optimizing sensor designs can be evaluated using the finite element simulations before making the actual prototype.

Sensors exploit a wide range of principles and in many cases the sensor principle depends directly upon the properties of the materials used in its construction. There is a variety of sensing materials, one of which is polyvinylidene fluoride (PVDF). A piezoelectric polymer that is used in a relatively new class of piezoelectric sensors. PVDF is a polymer that when stretched and poled in a high electric field produces a piezoelectric material [1–4].

1.1 Piezoelectricity Background

The piezoelectric effect is a natural phenomenon discovered by Pierre Curie and his brother Paul-Jean Curie in the 1880's [5]. They found that piezoelectric materials generate an electric charge when mechanically deformed and vice versa, i.e., when an external electric field is applied to piezoelectric materials they mechanically deform (change their physical dimensions). Piezoelectric devices are part of everyday life. They are in widespread use in consumer products, medical devices, office, industrial and military equipment. Even baseball bats are being outfitted with piezoelectric devices to reduce unwanted vibration. Large quantities of piezoelectric materials make-up the detection systems on submarines. In the medical field, piezoelectric materials produce the diagnostic images received via an ultrasound test. Piezoelectric applications also include switches, impact sensors, vibration sensing, speakers, microphones and accelerometers.

1.1.1 Piezoelectric Accelerometers

Piezoelectric accelerometers are the most widely used transducers for condition and vibration monitoring. They were first commercialized in the 1940's. They have no moving parts; are robust, easy to fit, have the widest frequency response and the benefit of low cost. Their output which is directly proportional to acceleration can be integrated to provide velocity and displacement units of measurement.

If an accelerometer is shaken back and forth in its sensitive plane, it generates an electric output which is proportional to the severity of shaking (the harder it shakes - the more it generates). The heart of a conventional piezoelectric accelerometer is a small piezo crystal which is bonded to a seismic mass. If the accelerometer is vibrated, the crystal is alternately compressed and decompressed between its outer case (attached to the machine) and the seismic mass whose inertia provides a resistance to

motion. The crystal generates an electrical signal proportional to vibration severity. This extremely low energy signal is converted by internal electronic circuitry into a useable voltage output, proportional to acceleration which can then be read by a data collector or an on-line system.

1.2 Basics of Piezo-Films

Piezoelectric materials have different forms and shapes, one of which is piezo-film sheets. Piezo-film is a flexible, lightweight, tough plastic film that is available in a variety of thicknesses and areas, besides its relative low cost. Hence, piezo-film seemed a reasonable choice for the construction of sensors.

Piezo-film is an anisotropic material since its electrical and mechanical responses differ depending upon the axis of applied mechanical stress or axis of electrical field. Axes of piezo-film are classified numerically by 1, 2 and 3 representing length (or stretch) direction, width (or transverse) direction and thickness direction, respectively as shown in Figure 1.1. As piezo-film is always thin, the electrodes are only applied

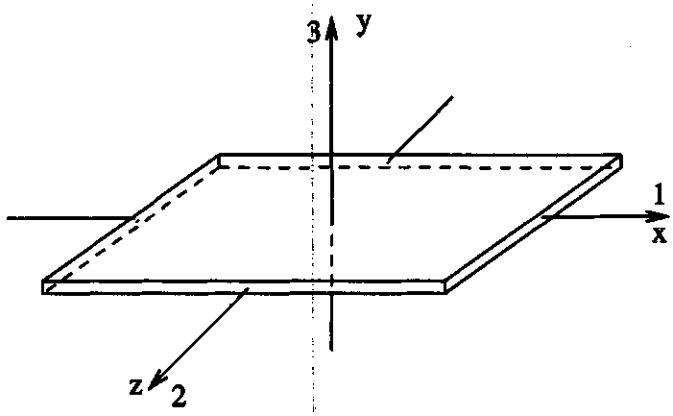

Figure 1.1: Numerical Classification of Piezo-Film Axes.

to the top and bottom film surfaces. Accordingly, the electrical axis is always in the

thickness direction as the charge or voltage is always transferred through the thickness of the film. The mechanical axis can be either in length, width or thickness directions indicated by 1, 2 or 3 directions depending on the applied stress. The most common piezo coefficients used are piezo strain constant, d_{3n} and piezo stress constant, g_{3n}, with the first subscript referring to the electrical axis, while the second subscript refers to the mechanical axis. Typically, Piezo-film is used in the mechanical '1' direction for low frequency sensing and actuation (<100 KHz) and in the mechanical '3' direction for high ultrasound sensing and actuation (>100 KHz). Table 1.1 shows some properties of a piezo-film material [5].

Table 1.1: Typical Properties of Piezo-Film.

Symbol	Parameter	PVDF	Units
h	Thickness	9, 28, 52, 110	μm
d_{31}	Piezo Strain Constant	23×10^{-12}	C/N
d_{33}	Piezo Strain Constant	-33×10^{-12}	C/N
g_{31}	Piezo Stress Constant	216×10^{-3}	Vm/N
g_{33}	Piezo Stress Constant	-330×10^{-3}	Vm/N
k_{31}	Electromechanical Coupling Factor	12 percent	
k_t	Electromechanical Coupling Factor	14 percent	
C	Capacitance	380 for 28 μm	pF/cm^2 @ 1KHz
Y	Young's Modulus	$2 - 4 \times 10^9$	N/m^2
P	Pyroelectric Coefficient	30×10^{-6}	C/m^2 ^{o}K
ϵ	Permitivity	$106 - 113 \times 10^{-12}$	F/m
ρ_m	Mass Density	1.78×10^3	Kg/m^3
	Yield Strength	$45 - 55 \times 10^6$	N/m^2

Typically piezo-films can convert signals in a variety of ways: electrical to mechanical (e.g., a loudspeaker), mechanical to electrical (microphone), and thermal to electrical (temperature sensor).

1.3 Mechanical to Electrical Energy Conversion

When a mechanical force is applied to a sheet of piezo-film in direction '3' (i.e., y-direction which is parallel to polarization), as shown in Figure 1.2, a voltage is generated which tries to return the piece to its original thickness. Similarly, when a force is applied to a sheet in directions '1' or '2' (i.e., x or z which are in this case perpendicular to polarization), a voltage is generated which tries to return the piece to its original width or length.

1.4 Sensor Modelling

Simulations are very useful for studying the piezoelectric effect, especially in developing small micro-machined components, when it is difficult to rely on experiments. Simulations offer several possibilities that are not easily realized with experiments.

Generally piezoelectric accelerometers have been modelled using analytical methods and with the advent of inexpensive and fast computers, numerical techniques using finite element analysis programs, can be used to predict and improve the performance of these devices.

1.5 Research Objective and Thesis Outline

This research was motivated by the need to develop a finite element model for a unique low cost, robust piezoelectric accelerometer [6]. The numerical results obtained were compared with the experimental and theoretical results. The stresses on the

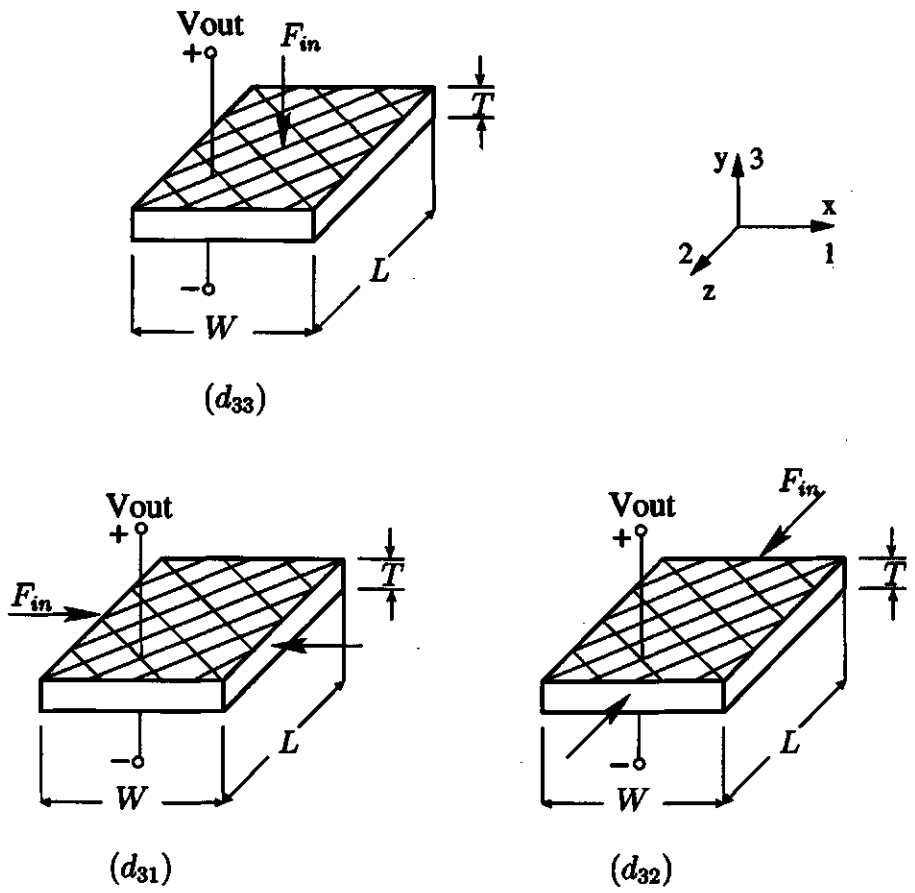

Figure 1.2: Piezo-Film Conversion of Force to Voltage.

sensing parts were investigated through the finite element model and compared to the yield strength of the materials used in the sensor, to ensure non breakage of the system. Also the finite element model could be easily and efficiently used to change some design parameters and study the effect of these variations on the systems' behavior before actually building it.

1.6 Review of Literature

In recent years, a growing interest towards the study of piezoelectric bodies has been devoted by the engineering practice. The main reason is the fact that piezoelectric materials are widely used as sensors and actuators in structure control problems. Piezo-films in particular are ideally suited as a sensor for use in active control of structural vibration, since they are flexible and easily shaped [7, 8].

A general review of piezo-film applications is given in [9], Chen et al stated that "Although the physical structure of piezoelectric transducer is relatively simple, it remains a challenge to construct a satisfactory transducer for a particular purpose".

A summary of the fundamental concepts in piezo-film technology and the physical properties of this material is presented in [10].

Generally, piezoelectric accelerometers have been modelled using analytical methods. Many excellent mathematical models exist for predicting the high-frequency response of piezoelectric transducers. Most of these, however, are designed to describe the behavior of thickness-mode devices [11]. Today with the large-scale production of the piezo-films, a new class of very useful transducers has arisen. And in many circumstances low-frequency response is of more concern than the upper limits [12].

Liu et al [13] stated that "with the advent of inexpensive and fast computers, numerical techniques have been developed rapidly which now can solve present-day

physical problems in engineering analysis and design. The finite element method is one such technique. It can be used flexibly to model any arbitrary geometry and characterize any given property of the material". Liu et al addressed another type of accelerometer (Brüel & Kjær) with different mode of operation.

Over the past few years, a significant amount of research has been conducted to study both the analytical and numerical models of different piezoelectric structures. Jan [14] used both approaches to treat piezoelectric low frequency resonators. Jenq et al [7], also used the two approaches to study the characterization of piezo-film sensors for direct vibration and impact measurements. Finite element models of laminated piezo-elastic structures [15], and smart piezoelectric shell structures [16] were also presented.

1.7 Organization of Thesis

In order to develop a suitable finite element model for the sensor, a deeper understanding could be gained from studying and manipulating its analytic expressions. A mathematical model [17], for the considered piezo-film sensor is presented in Chapter 2. Simulation of the analytical model was done via Simulink software and the simulated results were compared to the experimental results which were done in lab in previous work [18] using a data acquisition system.

Chapter 3 introduces the finite element method, its stages, and how the finite element model of the piezo-film sensor was developed. Analysis and results from the finite element method are discussed in Chapter 4. The numerical results, from the finite element analysis, are compared to experimental and theoretical results at the end of Chapter 4. Also some changes in the actual design were considered and studied. Chapter 5 includes the summary and suggestions for future work.

2. THEORETICAL MODEL FOR THE PIEZO-FILM SENSOR

2.1 Sensor Description

The basic construction of the piezo-film sensor is shown in Figure 2.1 and a cross-section of it is shown in Figure 2.3 [6]. The sensor consists of three pieces of plexiglass, two sheets of piezo-film and a copper cylinder (not shown in Figure 2.1 but shown in Figure 2.3). The copper cylinder has a diameter of 4.5 cm, and it consists of two

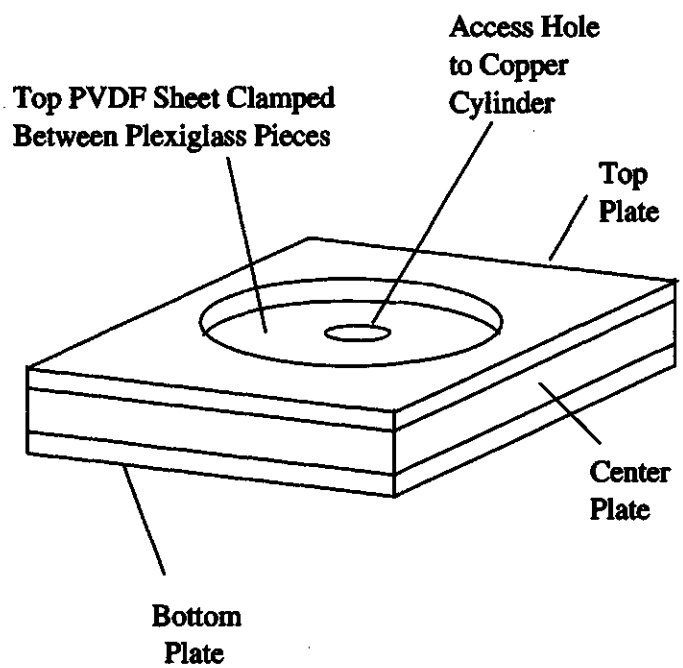

Figure 2.1: Piezo-Film Sensor.

solid threaded pieces that can be used to vary the thickness of the cylinder from

1.2 cm to 1.6 cm. This copper cylinder is inserted into the center of a 10 cm by 10 cm by 1.2 cm piece of plexiglass, referred to as the Center Plate in Figure 2.1, that has a 4.5 cm diameter hole drilled in it. The 8 cm by 8 cm piezo-film sheets are placed on the top and bottom of the Center Plate-Copper Cylinder combination. The two remaining 10 cm by 10 cm by 0.6 cm pieces of plexiglass, referred to as the Top and Bottom Plates in Figure 2.1, are screwed to the top and bottom of the structure to clamp the piezo-film sheets in place. These plates have a 6.4 cm circular hole drilled in their centers. Access to the copper cylinder is provided by two 0.5 cm holes cut in the center of the piezo-film sheets. These holes can be used to access the copper cylinder with screwdrivers to expand the cylinder creating a tight fit with the piezo-film sheets [6, 17].

As previously mentioned, the notation used to describe how the piezo-film is used in an application is an ordered pair of numbers, where the first number represents the electrical axis and the second represents the mechanical axis. This piezo-film sensor uses (3,1) mode. This mode produces the largest output voltage since the output is proportional to the stress and the piezo-film is very thin with a thickness of 110 μm.

The sensor is modelled with a system of second-order equation. The copper cylinder representing the mass and the two piezo-film sheets representing a spring. In the construction of the sensor, the piezo-film sheets are used both as a mechanical component of the sensor (the spring) and as the sensing element used to generate the electrical response [6, 17].

2.2 Sensor Model

A transducer is defined in *The Oxford Dictionary*, as a "device that converts one type of physical variable (eg.: force, pressure, temperature, velocity, flow rate, etc.)

into another form", while a sensor is a transducer that is used to make a measurement of the physical variable of interest [19, 20].

Piezo-film sensors are active transducers, directly converting applied mechanical energy into electrical energy. This electrical energy, in the form of induced surface charge, interacts with the capacitive electrodes to act as a voltage source.

The relationship between the acceleration $\gamma(t)$ and the output voltage $V(t)$ can be decomposed into two transfer functions as shown in Figure 2.2. A mechanical transfer function that gives the relation between the acceleration γ and the force F applied to the piezoelectric film represented by the mechanical transducer model block, and an electrical function that gives the relation between F and the output voltage V of the sensor represented by the electrical transducer model block [17].

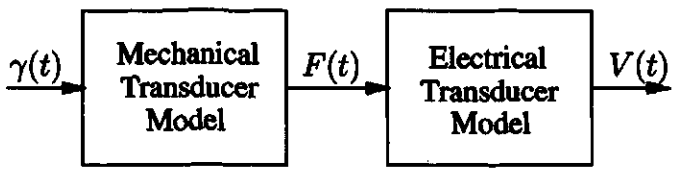

Figure 2.2: Sensor Model.

2.2.1 Mechanical Transducer Model

Figure 2.3 shows a cross-section of the sensor [17]. The mass, m, is a copper cylinder of radius r_1. The piezo-film supports are clamped between the plexiglass pieces a distance r_2 from the center of the transducer. The inset in Figure 2.3 shows an exaggerated view of the piezo-films relative to the mass and the plexiglass structure. The piezo-film cross-section in the inset is defined by the angle ϕ, x_d, which is the distance the mass m is above the plexiglass structure and $x_w = r_2 - r_1$.

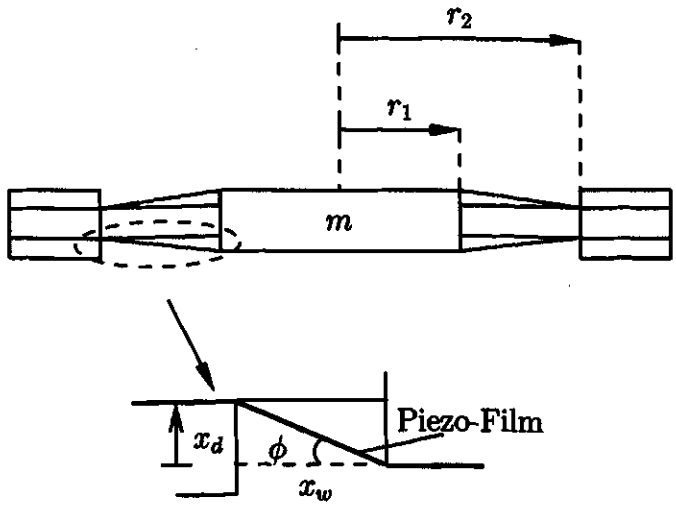

Figure 2.3: Center Cross-Section of Sensor with Inset Showing Piezo-Film Highlight (Not to Scale).

The sensor in Figure 2.3 can be modelled by the spring, mass and damper structure shown in Figure 2.4.

The spring constant, k, can be determined by examining the effect of a force on the transducer model. Figure 2.5a) shows part of the inset from Figure 2.3 with the piezo-film modelled as a spring with constant k_ϕ. F_ϕ is the component of the applied force F along the spring. Figure 2.5b) shows an equivalent model for Figure 2.5a).

Applying Hooke's Law in Figure 2.5b) gives

$$F = k_1 x_\delta, \tag{2.1}$$

and similarly for Figure 2.5a)

$$F_\phi = \frac{F}{sin\phi} = k_\phi x_\phi, \tag{2.2}$$

where k_ϕ is the piezo-film spring constant and x_ϕ (not shown in the figure) is the

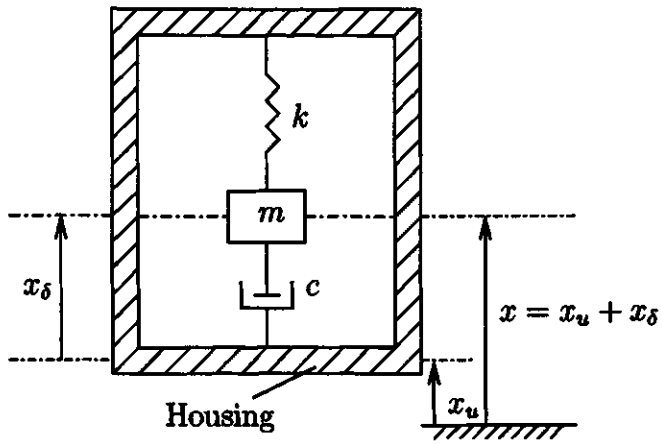

Figure 2.4: Mechanical Accelerometer Model.

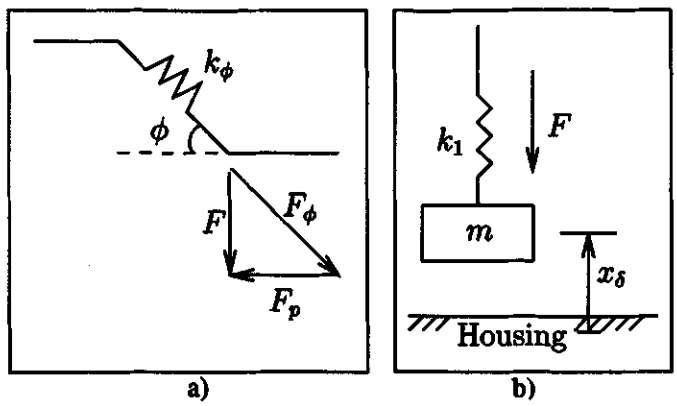

Figure 2.5: Mechanical Model for Piezo-Film Spring.

displacement due to the force F_ϕ. Equating equations (2.1) and (2.2) gives

$$k_1 = k_\phi sin\phi \frac{x_\phi}{x_\delta} = k_\phi sin^2\phi, \tag{2.3}$$

where for small x_δ displacements $\sin\phi \simeq x_\phi / x_\delta$. Similarly the upper piezo-film support gives $k_2 = k_\phi sin^2\phi$, thus k in the model of Figure 2.4 is given by

$$k = k_1 + k_2 = 2k_\phi sin^2\phi. \tag{2.4}$$

In Figure 2.4, a displacement motion x_u of the sensor housing will produce a

relative displacement between the mass and the case of x_δ. The movement of the mass with respect to the fixed reference is $x(t) = x_u(t) + x_\delta(t)$. The force causing the acceleration of the mass, m, is md^2x/dt^2 and thus the force applied by the mass to the spring and damper is $-md^2(x_u+x_\delta)/dt^2$. The force applied by the spring is $-kx_\delta$ and the force applied by the damper is $-cdx_\delta/dt$, where c is the damping coefficient. Summing these forces, which sum to zero, and simplifying gives

$$m\gamma(t) = m\frac{d^2x_u}{dt^2} = -(m\frac{d^2x_\delta}{dt^2} + c\frac{dx_\delta}{dt} + kx_\delta(t)), \tag{2.5}$$

where $\gamma(t)$ is defined as the acceleration of the transducer unit.

The piezo-film is the sensing element producing an output that is proportional to the force, thus it is modelled as a spring where the applied force is defined by

$$F(t) = kx_\delta(t) = 2k_\phi sin^2\phi x_\delta(t), \tag{2.6}$$

using Equation (2.4).

The constant k_ϕ can be determined using the relation

$$k_\phi = \frac{YA}{l}, \tag{2.7}$$

where Y is the Young's modulus of the piezo-film, A and l are the cross sectional area and the length of the piezo-film sheet, respectively. Since the piezo-film supporting structure is circular, calculating k_ϕ requires specific attention [17]. The circular structure can be viewed as N springs in series. These springs have a cross-sectional area of $2\pi rh$ where r is the radial distance, which varies from r_1 to r_2. The length of each of these springs is Δr, where $\Delta r = \frac{r_2-r_1}{N}$. In the limit as Δr becomes very small, the equivalent spring constant of this circular structure is

$$k_\phi = \frac{1}{\int_{r_1}^{r_2}\frac{dr}{2\pi rhY}} = \frac{2\pi hY}{\ln(r_2)-\ln(r_1)} = \frac{2\pi hY}{\ln\left(\frac{r_2}{r_1}\right)}. \tag{2.8}$$

2.2.2 Electrical Transducer Model

The electrical transducer model can be simplified as shown in Figure 2.6 [17]. The Piezo Component block in Figure 2.6 transforms the applied force, $F(t)$, to the charge $Q(t)$ developed on the piezo-film electrodes. The Electronic Component block in Figure 2.6, transforms the charge $Q(t)$ into the output voltage $V(t)$.

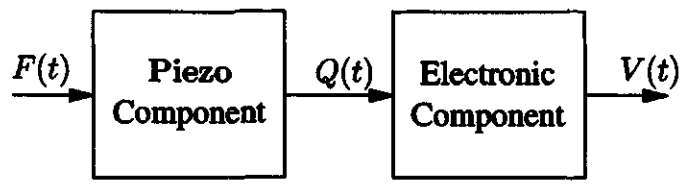

Figure 2.6: Electrical Model.

Starting with the Piezo Component block, it is important in the development of the block model to recognize where the applied force is acting on the piezo-films. Referring to Figure 2.5a), the applied force F consists of two components, F_p and F_ϕ. F_p is acting on the section of the piezo-film in direct contact with the copper mass. It is assumed that F_p has little effect on the piezo-film because it is being cancelled by the frictional force between the piezo-film and mass, with the friction at the corners dominating. F_ϕ, in Figure 2.5a), produces a stress that acts along direction 1. The stress in the other piezo-film directions is assumed to be very small and thus is not considered in the following development for $Q(t)$ [17].

The piezoelectric characteristics can be described as a constitutive relation which characterizes the coupling effect between mechanical and electrical properties as follows:

$$S_p = s^E_{pq} T_q + d_{ip} E_i \qquad p, q = 1, ..., 6 \tag{2.9}$$

$$D_i = d_{iq} T_q + \epsilon^T_{ik} E_k \qquad i, k = 1, 2, 3 \tag{2.10}$$

where S_p and T_q represent the strain and stress respectively. D_i and E_k are the respective electric flux density and electric field intensity. s_{pq}^E is the elastic constant at constant electric field, d_{ip} is the piezoelectric strain constant, and $\epsilon_{ik}^T$is the electric permittivity at constant stress. The subscripts can take on the values $p, q = 1, ..., 6$ and $i, k = 1, 2, 3$ where 1, 2, 3 are the directions previously defined and they are associated with axes x, z, y and indices 4, 5, 6 represent rotations about these axes [21, 22].

In defining these equations, it is important to select the independent variables for the mechanical and electrical action. The mechanical action is along the '1' direction, since the piezo-film is being stretched by the force F_ϕ. The tensile stress, T_1, is the only significant stress since $T_2, T_3 \simeq 0$, thus T_1 is the best choice for the independent mechanical variable. The electrical action independent variable is the electric field, E_3, since for piezo-film the electrodes are on the direction '3' surfaces and the electric field is constant in directions parallel to the electrode surfaces. The electric flux density is only constant in directions perpendicular to the electrode surfaces [17].

Using these simplifications the piezoelectric equations for this system are

$$S_1 = s_{31}^E T_1 + d_{31} E_3$$

$$D_3 = d_{31} T_1 + \epsilon_{33}^T E_3, \tag{2.11}$$

where d_{31} is the piezoelectric constant in direction '1', ϵ_{33}^T is the dielectric constant where the T superscript indicates constant stress, s_{31}^E is the elastic compliance where the E superscript indicates constant electric field, E_3 is the electric field and T_1 is the stress in the '1' direction. The stress, T_1, is determined using

$$T_1 = \frac{F}{A_r},$$

where A_r is the average cross-section area of the piezo-film in the ring between radial

distance r_1 and r_2 of Figure 2.3. The average area is given by

$$A_r = \frac{\int_{r_1}^{r_2} 2\pi h r dr}{r_2 - r_1} = \frac{h\pi(r_2^2 - r_1^2)}{r_2 - r_1} = h\pi(r_1 + r_2),$$

and the stress is

$$T_1 = \frac{F}{h\pi(r_1 + r_2)}. \tag{2.12}$$

The uniform electric field is given by

$$E_3 = \frac{-dV}{dh} = \frac{-V}{h}. \tag{2.13}$$

Substituting (2.12) and (2.13) into (2.11) gives

$$D_3 = \frac{d_{31}}{\pi h(r_1 + r_2)} F - \frac{\epsilon_{33}^T}{h} V.$$

A variation of the stress T_1 gives a charge Q across the film

$$Q = D_3 A_\phi = D_3 \pi(r_2^2 - r_1^2)$$

$$= \frac{d_{31}}{h}(r_2 - r_1)F - \frac{\epsilon_{33}^T}{h}\pi(r_2^2 - r_1^2)V, \tag{2.14}$$

where A_ϕ is the surface area of the section of piezo-film producing the charge, Q.

The second block in Figure 2.6, the Electronic Component block transforms the charge $Q(t)$ into the output voltage $V(t)$ [17]. Physically, this block consists of the piezo-film which is connected to the input of a voltage follower operational amplifier circuit. The complete piece of piezo-film, which has a surface area of A_c and a thickness of h, can be modelled as a capacitor, $C_p = \epsilon_{33}^T A_c/h$, in parallel with a resistor, $R_p = \rho h/A_c$, where ρ is the resistivity of the piezo-film. The equivalent circuit for the input to the voltage follower is also a parallel combination of the input capacitance C_i and the input resistance R_i. Combining the equivalent circuits for the piezo-film and voltage follower gives the model of the Electronic Component block.

This model consists of the parallel combination of the equivalent resistor, R_{eq} and the equivalent capacitor, C_{eq}, where

$$R_{eq} = \frac{R_p + R_i}{R_p R_i},$$

and

$$C_{eq} = C_p + C_i. \tag{2.15}$$

The equivalent capacitor, C_{eq} must be incorporated into Equation (2.14) since it will affect the charge, Q.

The electrical response is given by the second term in Equation (2.14),

$$\frac{C_p \pi}{A_c}(r_2^2 - r_1^2)V \tag{2.16}$$

where C_p has been substituted. Since C_p is in parallel with C_i, a portion of the charge must be on C_i, reducing the charge on the film. Replacing C_p with C_{eq} in (2.16) will account for this reduction, to give

$$Q = \frac{d_{31}}{h}(r_2 - r_1)F - \frac{C_{eq}\pi}{A_c}(r_2^2 - r_1^2)V.$$

The output voltage, $V(t)$ is defined by the current dQ/dt through R_{eq} as

$$V = R_{eq}\frac{dQ}{dt},$$

$$V = \frac{R_{eq} d_{31}}{h}(r_2 - r_1)\dot{F} - \frac{R_{eq} C_{eq}}{A_c}\pi(r_2^2 - r_1^2)\dot{V}, \tag{2.17}$$

where $\dot{F} = dF/dt$ and $\dot{V} = dV/dt$. Rearranging Equation (2.17) gives

$$\dot{V} = -K_v V + K_f \dot{F}, \tag{2.18}$$

where

$$K_v = \frac{A_c}{R_{eq} C_{eq} \pi (r_2^2 - r_1^2)}, \tag{2.19}$$

$$K_f = \frac{d_{31} A_c}{C_{eq} h \pi (r_1 + r_2)}. \tag{2.20}$$

2.2.3 Sensor Transfer Function

The system transfer function for the sensor model shown in Figure 2.2 is given by

$$H(s) = H_{mm}(s)H_{em}(s),$$

where $H_{mm}(s) = F(s)/\gamma(s)$ is the mechanical model transfer function and $H_{em}(s) = V(s)/F(s)$ is the electrical model transfer function [17]. The mechanical model transfer function can be determined by taking the Laplace transform of Equations (2.5) and (2.6), and taking the ratio $F(s)/\gamma(s)$ and simplifying to give

$$H_{mm}(s) = \frac{k}{s^2 + \frac{c}{m}s + \frac{k}{m}}.$$

This equation can be put into a standard second order form as

$$H_{mm}(s) = m\frac{\omega_n^2}{s^2 + 2\xi\omega_n s + \omega_n^2}, \tag{2.21}$$

where $\omega_n = \sqrt{k/m}$ is the undamped natural radian frequency and $\zeta = c/(2\sqrt{km})$ is the damping ratio.

The electrical model transfer function can be determined from the Laplace transform of Equation (2.18) to give

$$H_{em}(s) = K_f\frac{\frac{1}{K_v}s}{1 + \frac{1}{K_v}s}. \tag{2.22}$$

From equations (2.21) and (2.22), we can obtain the global transfer function of the transducer

$$H(s) = (mK_f)\left(\frac{\frac{1}{K_v}s}{1 + \frac{1}{K_v}s}\right)\left(\frac{\omega_n^2}{s^2 + 2\xi\omega_n s + \omega_n^2}\right). \tag{2.23}$$

The characteristics of the system are defined by the three terms in parentheses in Equation (2.23). The first term $K_s = mK_f$ defines the passband sensor sensitivity. The second term is due to the electrical model, and it represents a high pass filter

with low cutoff frequency, K_v radian/second. The third term is due to the mechanical model and it is an underdamped, resonant, low pass system (for $\zeta < 1/\sqrt{2}$) with a resonant frequency of $\omega_r = \omega_n\sqrt{1-2\zeta^2}$ [17].

2.3 Experimental/Theoretical Results

Characteristics of the piezo-film sensor [17]:

1. Mass, $m = 0.1844$ Kg
2. Piezo-film Area, $A_c = 6400\ \mu\text{m}^2$
3. Piezo-film Thickness, $h = 110\ \mu$m
4. Outer radius, $r_2 = 0.032$ m
5. Inner radius, $r_1 = 0.0225$ m
6. Mass Distance, $x_d = 1750\ \mu$m
7. Input resistance, $R_i = 100\ \text{M}\Omega$
8. Input capacitance, $C_i = 5.5$ pF.

The experimental results were generated using a Bruel & Kjaer Type 4809 Vibration Exciter and a Bruel & Kjaer Type 4370 reference accelerometer, which was calibrated using a Bruel & Kjaer Calibration Exciter Type 4294 [6]. The input acceleration was set to $\gamma(t) = 0.5\ \text{m/s}^2$. The experimental results are plotted as the dotted line in Figure 2.7 [17].

The small peak in Figure 2.7 is likely caused by the threaded mass, which consists of two pieces of copper that are not perfectly rigid. The existence of this small peak

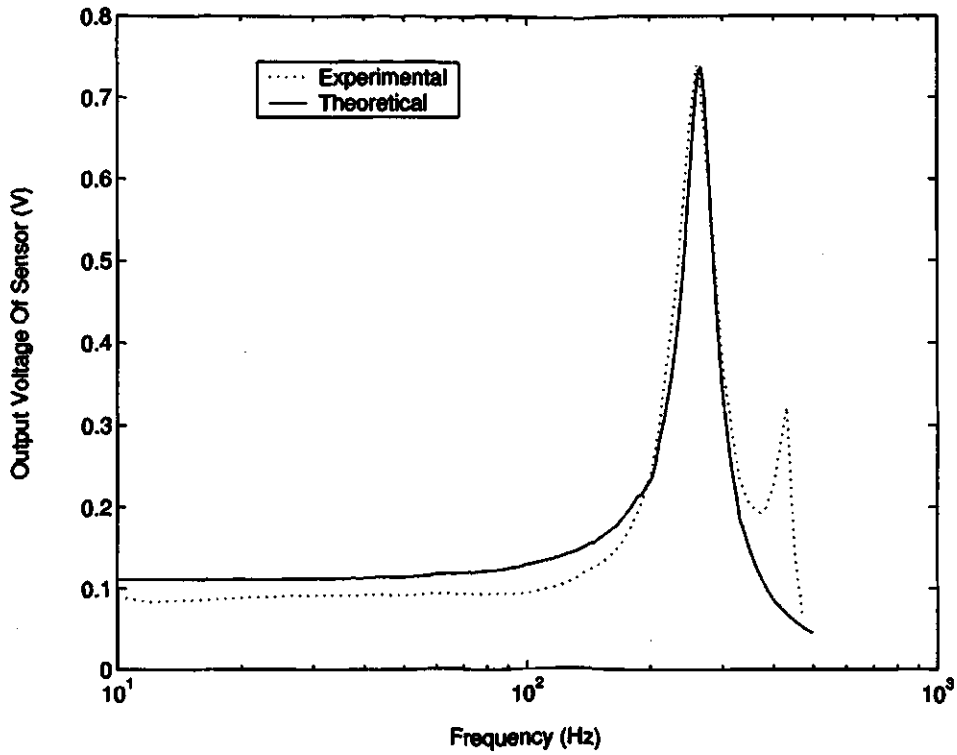

Figure 2.7: Comparison Between Experimental and Theoretical Results for an Acceleration of $\gamma(t) = 0.5$ m/s^2.

is viewed as a minor concern, since for an accelerometer, the region of interest occurs to the left of the resonance peak.

The theoretical results are generated using the following piezo-film constants from Table 1.1 in Chapter 1.

1. Young's Modulus, $Y = 4 \times 10^9$ N/m^2
2. Dielectric Constant, $\epsilon_{33}^T = 113 \times 10^{-12}$ F/m
3. Strain Constant, $d_{31} = 23 \times 10^{-12}$ C/m^2/N/m^2

4. Resistivity, $\rho = 1 \times 10^{13}$ Ωm.

Calculating the various system constants gives [17]

1. $C_p = \epsilon_{33}^T A_c/h = 6.58$ nF
2. $R_p = \rho h/A_c = 1.72 \times 10^{11}$ Ω
3. k from Equation (2.4), $k = 5.15 \times 10^5$ N/m
4. K_v from Equation (2.19), $K_v = 5.99$
5. K_f from Equation (2.20), $K_f = 1.19$
6. $\omega_{n_{th}} = \sqrt{k/m} = 1671.5$ radian/sec.

The theoretical simulation was implemented using the software tool Simulink [23]. This tool was used to perform time-based simulation of Equations (2.5), (2.6) and (2.18). Figure 2.8 shows the block diagram of the Simulink model used, where the input is a sinusoidal wave representing the input acceleration to the system.

The circular blocks represent summers used to add up the different terms. The square blocks with '$\frac{1}{S}$' are integrators, the triangular blocks are simple multipliers (gain) and the *Wk.Space* block is the work space for storing the output.

The frequency response indicated by the solid line in Figure 2.7 was generated by varying the frequency of the input in the Simulink model. This response is equivalent to the response in Equation (2.23).

The close correspondence between the two curves in Figure 2.7 is remarkable. The passband sensitivity for the model is $K_s = 0.2192$ V/m/s^2 (calculated from the first term in Equation (2.23), $K_s = mK_f$) over a frequency range of 10 and 100

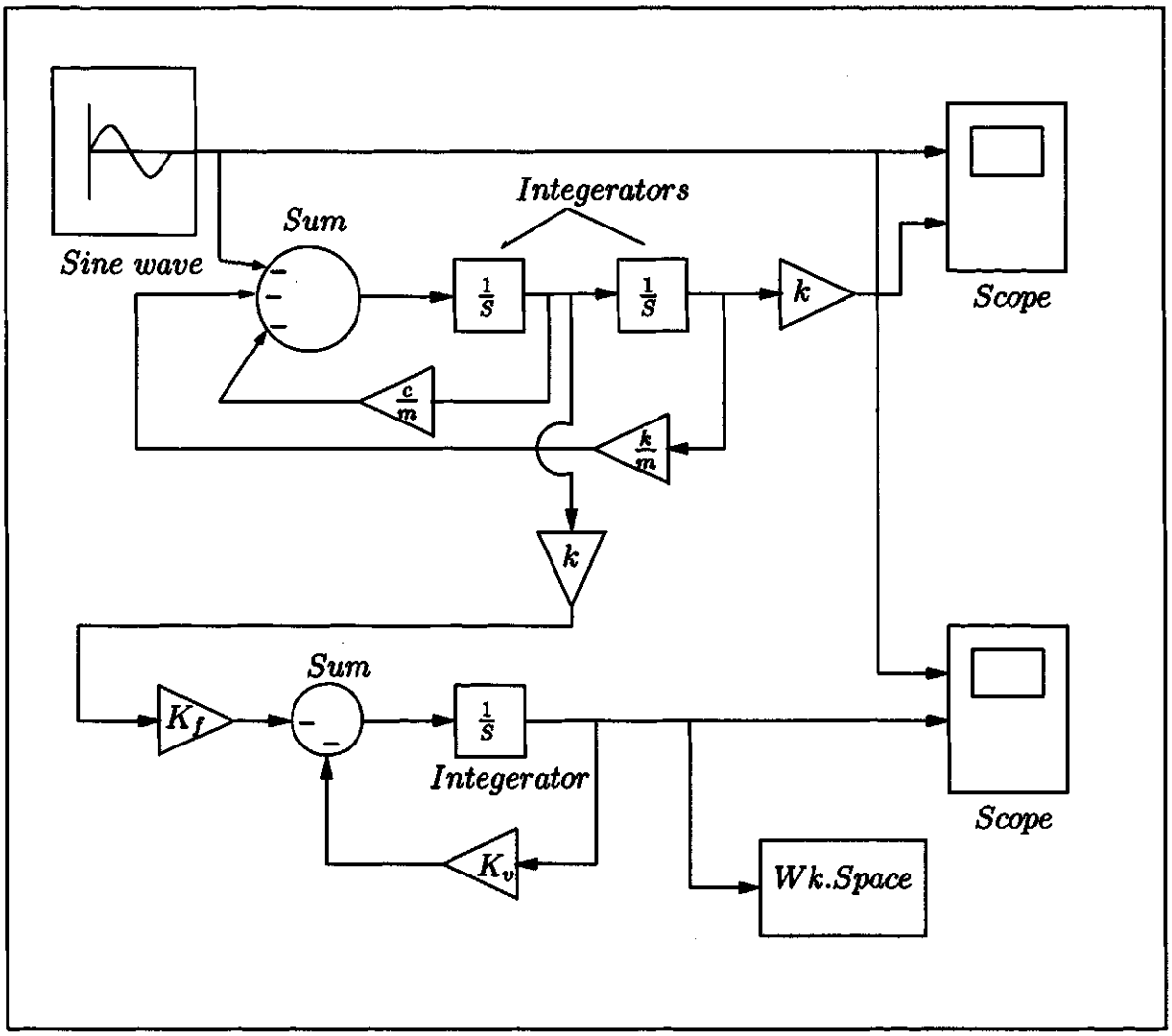

Figure 2.8: Block Diagram of the Simulink Model.

Hz. The experimental results for the passband sensitivity is somewhat less than 0.2 $V/m/s^2$ though it is relatively constant over the frequency range of 10 and 100 Hz. The difference in sensitivities is likely due to the unaccounted frictional forces on the copper mass [17].

2.4 Parameter Relationships

The sensor under study had a sensitivity of $K_s = 0.2192$ V/m/s^2 and a natural frequency of $\omega_n = 1671.5$ radian/sec. These important characteristics of the sensor are defined by the construction parameters, specifically, x_d, m, r_2 and r_1. This can be demonstrated by simplifying the expression for K_s and ω_n [17].

$$K_s = mK_f = \frac{md_{31}A_c}{C_{eq}h\pi(r_1 + r_2)},$$

using Equation (2.20) and since $C_p \gg C_i$

$$K_s \simeq \frac{md_{31}}{\epsilon_{33}^T \pi(r_1 + r_2)}. \tag{2.24}$$

Thus

$$K_s \propto \frac{m}{r_1 + r_2} \tag{2.25}$$

since the other terms in Equation (2.24) are constants. For ω_n,

$$\omega_n = \sqrt{k/m} = \sqrt{\frac{4\pi hY \sin^2\phi}{m \ln(r_2/r_1)}}, \tag{2.26}$$

using Equations (2.4) and (2.8), and since

$$\sin\phi = \frac{x_d}{\sqrt{x_d^2 + x_w^2}} \simeq \frac{x_d}{(r_2 - r_1)}$$

where $x_w \gg x_d$, Equation (2.26) can be simplified to

$$\omega_n \simeq \sqrt{\frac{4\pi hY x_d^2}{m(r_2 - r_1)^2 \ln(r_2/r_1)}}. \tag{2.27}$$

Thus

$$\omega_n \propto \frac{x_d}{(r_2 - r_1)\sqrt{m \ln(r_2/r_1)}}, \tag{2.28}$$

since the other terms in (2.27) are constants [17].

Equations (2.25) and (2.28) clarify the dependencies for this sensor construction. For example, to increase the bandwidth of the sensor under study, the simplest

approach would be to increase x_d, which is defined in Figure 2.3. Increasing x_d in Equation (2.28) by a factor of 2, to 3.5 millimeters, will approximately double ω_n [17]. Simulating the sensor via simulink, the curve in Figure 2.9 is generated with a natural frequency of about 507 Hz.

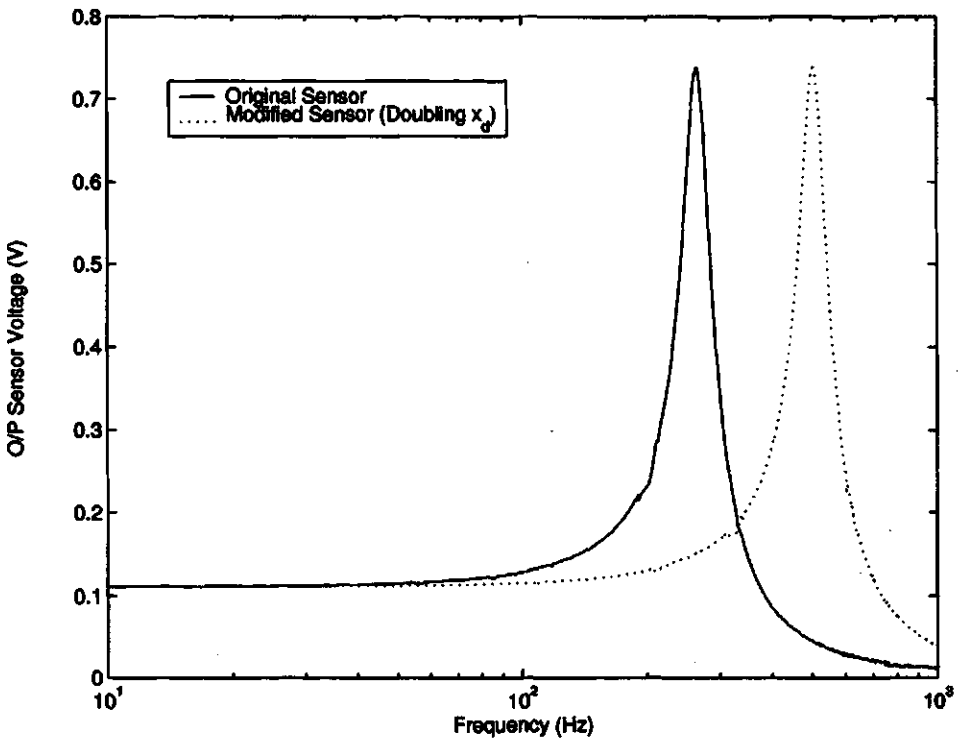

Figure 2.9: Variation of Output Voltage with Frequency for Original and Doubled x_d Sensors via Simulink.

Another example involves reducing the size of the sensor. If r_1 and r_2 are both decreased by factor of 2 with the mass remaining the same, ω_n will be approximately double according to Equation (2.28) [17]. Using Simulink, the natural frequency increased to 507 Hz and K_s increased by a factor of 2 approximately ($K_s = 0.4426$)

as shown in Figure 2.10. All of the above results are generated using an acceleration of 0.5 m/s^2.

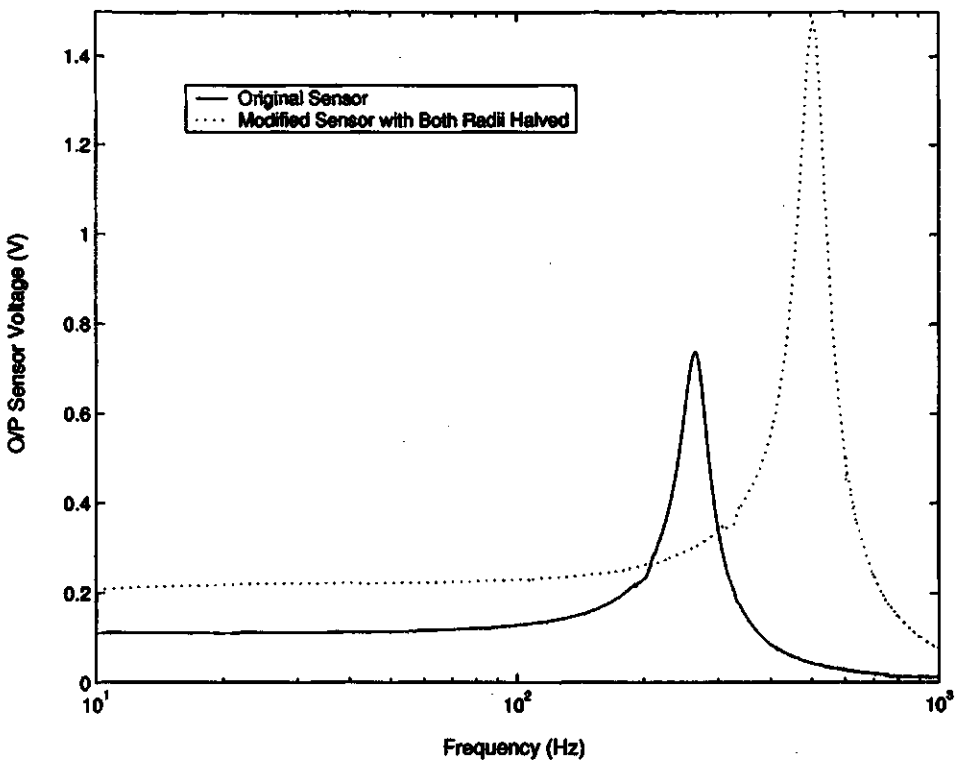

Figure 2.10: Variation of Output Voltage with Frequency for Original and Both Radii Halved Sensors via Simulink.

3. FINITE ELEMENT MODEL

3.1 Finite Element Method

The Finite Element Method (FEM), also called FEA (Finite Element Analysis), is a numerical technique, well suited to digital computers, that can be applied to solve problems in solid mechanics, fluid mechanics, heat transfer and vibrations. The main idea of FEM is to break a complicated problem or divide the actual geometry of the structure into small pieces (elements) of a finite size. These elements are connected at points called nodes. The collection of nodes and finite elements known as the mesh is shown in Figure 3.1.

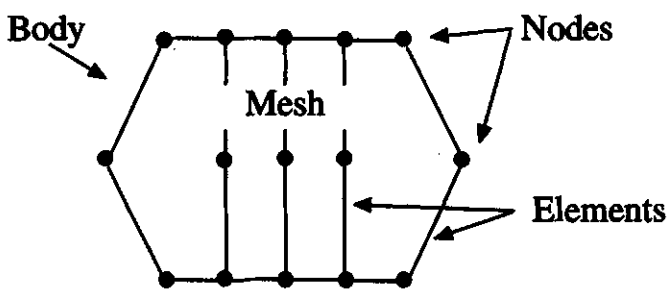

Figure 3.1: Mesh.

Each piece is considered to be part of the main problem, and for the small element itself, the internal physical laws (i.e., Hooke's law for elastic deformation problems) can be simplified, because the element shape is simple, mostly a triangle or a quadrilateral. The global problem can be transformed into a matrix of simple element equations which are connected by the condition that common nodes undergo the

same change of global state. In solids models, displacements in each element are directly related to the nodal displacements. The nodal displacements are then related to the strains and the stresses in the elements. The finite element method tries to choose the nodal displacements so that the stresses are in equilibrium (approximately) with the applied loads. The nodal displacements must also be consistent with any constraints on the motion of the structure.

The finite element method converts the conditions of equilibrium into a set of linear algebraic equations for the nodal displacements that can be easily solved by computer. Once the equations are solved, one can find the actual strains and stresses in all the elements. By breaking the structure into a larger number of smaller elements, the stresses become closer to achieving equilibrium with the applied loads. Therefore an important concept in the use of finite element methods is that, in general, a finite element model approaches the true solution to the problem only as the element density is increased within the availability of computer power [24–28].

3.2 Basics of FEA

A typical finite element analysis consists of three phases, as indicated in Figure 3.2. The pre-processing phase consists of specifying and checking the input data. This is followed by the solution phase in which the analysis is carried out. The final phase, which is known as the post-processing phase, is concerned with the interpretation and presentation of the results and analysis.

3.2.1 Pre-processing

There are a number of steps in the pre-processing phase of FEA. All finite element packages need to go through these steps in one form or another.

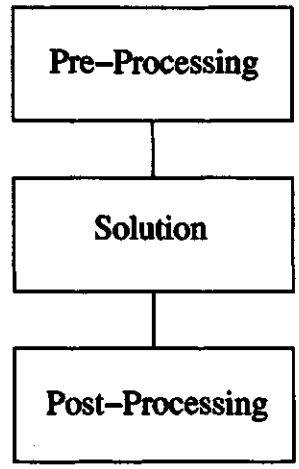

Figure 3.2: Finite Element Procedure.

1) *Specify geometry:* first the geometry of the structure to be analyzed is defined. This can be done either by entering the geometric information in the finite element package through the keyboard or mouse, or by importing the model from a solid modeler like CAD.

2) *Specify material properties:* next, the material properties are defined. In an elastic analysis of an isotropic solid these consist of the Young's modulus, the density, and the Poisson's ratio of the material.

3) *Mesh the object:* then, the structure is broken (or meshed) into small elements. This involves defining the types of elements into which the structure will be broken, as well as specifying how the structure will be subdivided into elements (how it will be meshed). This subdivision into elements can either be input by the user or, with some finite element programs can be chosen automatically by the computer based on the geometry of the structure (this is called automeshing).

4) *Apply Boundary Conditions:* next, the boundary conditions and the external loads are specified.

3.2.2 Solution Phase

Once the input has been prepared, the solution can be carried out. Figure 3.3 shows the various types of analysis [27]. For forced response the first choice is between a modal solution (M) or a direct solution (D). For a modal solution the frequencies and modes of free vibration have to be calculated first. In either case, the next choice is between a frequency (F) or time domain (T) solution. In the frequency domain, harmonic response is a prerequisite to both periodic (P) and random response (R) as well as being an important solution procedure itself (harmonic response analysis seeks the amplitude of response when prescribed loads vary sinusoidally with time). In the time domain the choice is between a time history of the response (TH) or predicting the peak response using the response spectrum method (RS). Time history (TH) analysis, also called transient response analysis or dynamic response analysis, is the calculation of how a structure responds to arbitrary time-dependent loading. It seeks the maximum displacement, acceleration or stress at a certain location in the structure, without regard to the time at which the maximum occurs. While the response spectrum (RS), is in general, a plot of the maximum value of some response (displacement, velocity or acceleration) versus frequency.

Typically finite element programs carry out further checks on the data during the solution phase. Fatal errors will cause the execution to be terminated. Non-fatal errors will be indicated by warning messages, but execution will continue [27, 28].

3.2.3 Post-processing

Based on the initial conditions and applied loads, data is returned after a solution is processed. This data can be viewed in a variety of graphs and displays.

Since the finite element solution technique is a numerical approximate procedure,

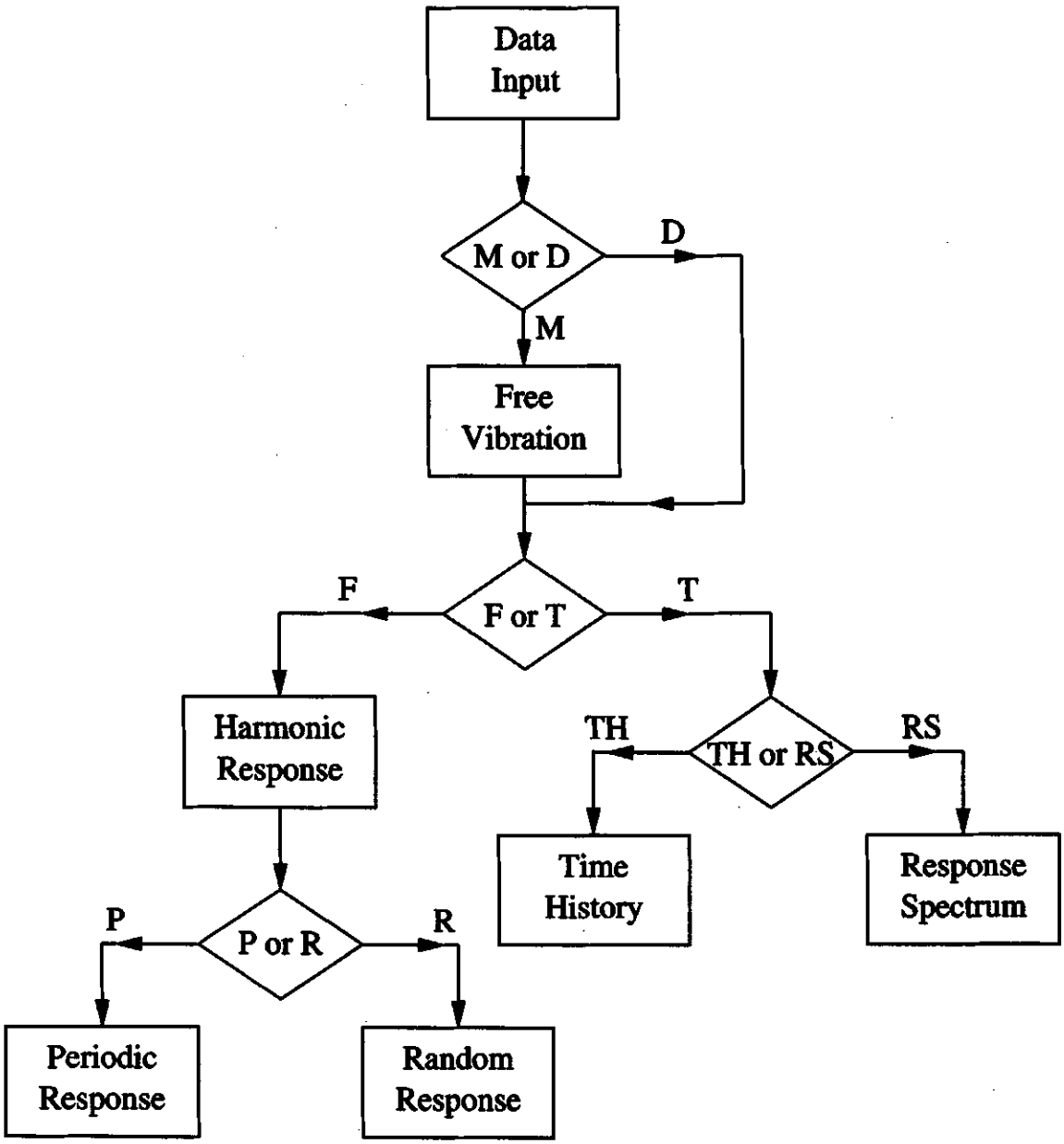

Figure 3.3: Flow Chart of Solution Phase.

it is necessary to assess the solution accuracy. In general, the accuracy of the approximation increases with the number of elements used. The number of elements needed for an accurate model depends on the problem and the specific results to be extracted from it. Thus, in order to judge the accuracy of results from a single finite element run, the number of elements in the model should be increased and check its effect on the results.

Once a mathematical model has been solved accurately and the results have been interpreted, changes in the physical problem could be considered. This in turn will lead to additional mathematical models and finite element solutions. Figure 3.4 summarizes the process of finite element analysis [29].

3.3 Computer Programs for FEM

There are two general approaches to the solution of problems by the finite element method. One is to use large commercial programs, many of which have been configured to run on personal computers (PCs); these general-purpose programs are designed to solve many types of problems. The other is to develop many small, special-purpose programs to solve specific problems.

There are numerous vendors supporting finite element programs such as

1. Algor
2. ANSYS
3. COSMOS/M
4. ADINA
5. SAP90

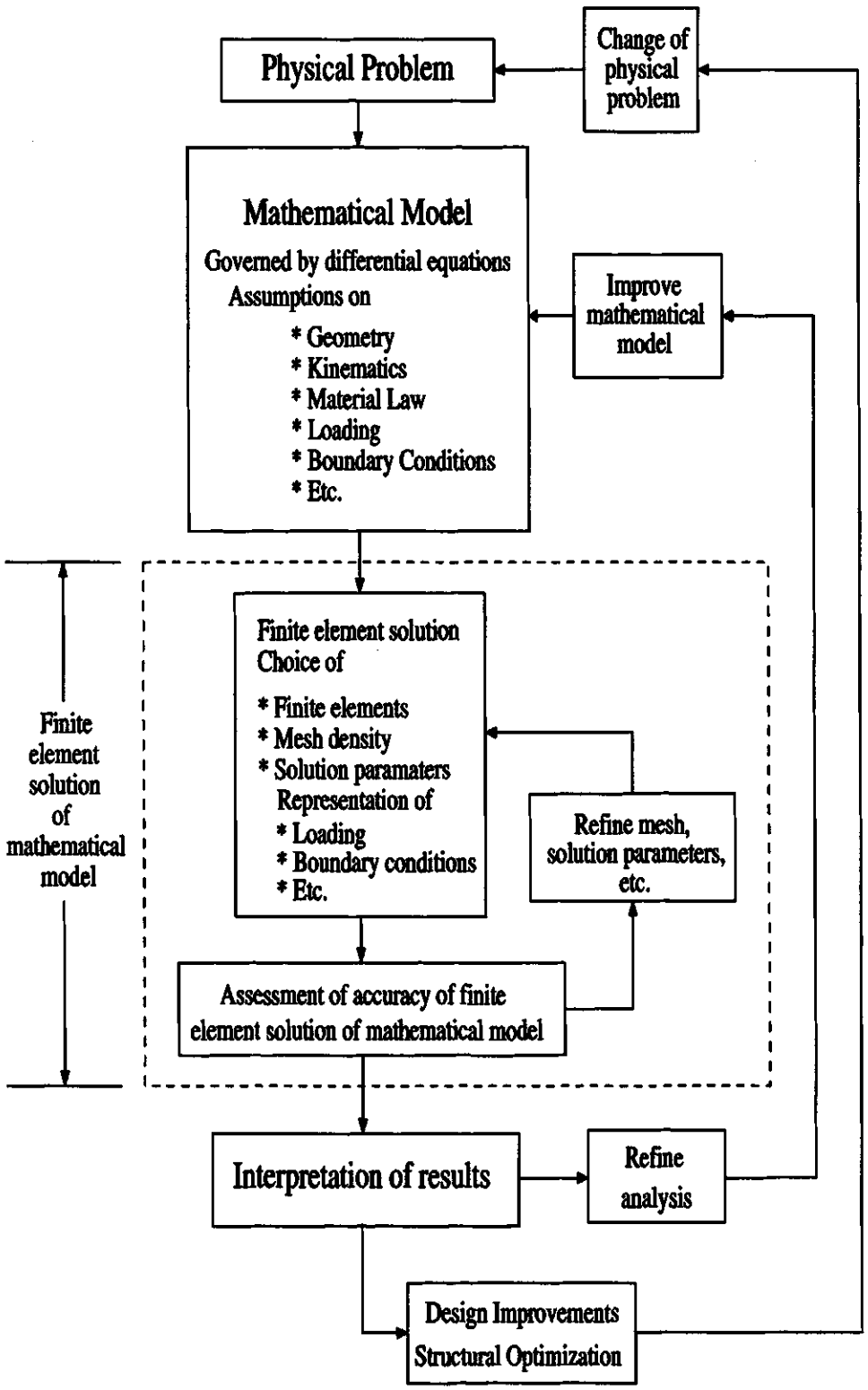

Figure 3.4: Block Diagram of Finite Element Analysis.

and many more. Standard capabilities of these programs include information on

1. Element types available, such as beam, plane stress and 3-dimensional solid.

2. Types of analysis available, such as static or dynamic.

3. Material behavior, such as linear-elastic and nonlinear.

4. Load types, such as concentrated, distributed, thermal, and displacement.

5. Data generation, such as automatic generation of nodes and elements (most programs have pre-processors to generate the mesh for the model).

6. Plotting, such as original and deformed geometry and stress and temperature contours (most programs have post-processors to aid in interpreting results in graphical form).

7. Displacement behavior, such as small and large displacement buckling.

8. Selective output, such as at selected nodes, elements, and maximum or minimum values.

In this study, ADINA was chosen as it deals mostly with dynamic structures.

3.4 ADINA

ADINA R & D, Inc. was founded in 1986 by Dr. K. J. Bathe and associates. The ADINA system solves a wide variety of problems in structural, thermal and fluid flow analysis [30]. For the structural analysis, ADINA system includes:

* the pre-processor ADINA-IN,

* the structural analysis ADINA, and

* the post-processor ADINA-PLOT.

In the ADINA-IN, it is necessary to completely describe the model, including the geometry of the model, material properties, boundary conditions and loads. It is also necessary to divide the model into finite elements and to define nodes. In ADINA-IN, the model, boundary conditions and loads could be displayed. ADINA-IN creates data files containing the finite element model definition and these files are used as input to the solution program ADINA. This solution program runs in the background. This program produces "porthole" files containing the model definition and the model results. Porthole files are then loaded in ADINA-PLOT to examine the results, for example, to plot deformed meshes, contours of filled bands of results such as stresses, vector plots of results such as reactions, velocities or stresses. Also graphing time histories of the results or results along a line within a model could be plotted.

3.4.1 FE Model in ADINA

Developing a finite element model in ADINA involves several steps as follows:

1. Definition of the "geometry model", which defines the problem to be solved but does not actually contain any finite elements, by defining the geometry which can be imported from another program and/or defined using ADINA-IN, defining the loads, material properties, boundary conditions, initial conditions and element properties.

2. Definition of the finite element model from the geometry model. This is done by defining any element groups to be used in the meshing process. Determining the subdivision data throughout the geometry, and finally meshing the geometry model.

3. Choice of the solution program and analysis type according to the results and analysis needed.

4. Finally, generation of a solution program data file.

Detailed explanation of each of the previous steps will be presented while devel-

oping the sensor model under study. For a simple detailed example see Appendix A.

3.5 Sensor Model Definition

The piezo-film sensor described in Chapter 2 is replaced by a simplified structure which retains the essential features to be investigated. It consists of 2 circular piezo-film sheets and a copper mass between them as shown in Figure 3.5.

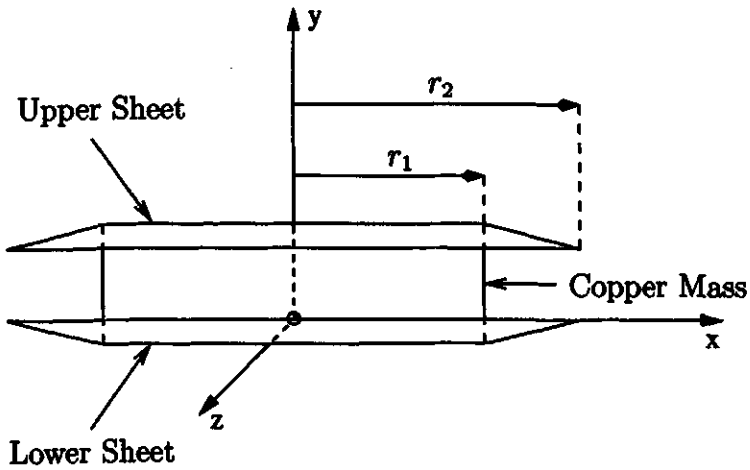

Figure 3.5: Simplified Sensor Model (Not to Scale).

3.5.1 Defining the Geometry

Geometry points, geometry lines, geometry surfaces and geometry volumes of a model are defined in the ADINA User Interface (AUI). AUI provides a user-friendly window based environment in which finite element models are constructed, analyzed and displayed.

Defining Coordinate System

In ADINA package, coordinate systems can be cartesian, cylindrical or spherical, also they can be either global or local. For this study, global cartesian coordinate system was selected.

Defining Geometry Points

Geometry points have single locations in space, which are defined by x, y, and z coordinates. Each geometry point is assigned a number which labels the point. It is worth noting that the geometry points and the finite element nodes are completely distinct. The AUI may or may not generate nodes at geometry point locations.

The piezo-film sensor has been defined using 22 points, the first 10 points defining the lower sheet are shown in Figure 3.6.

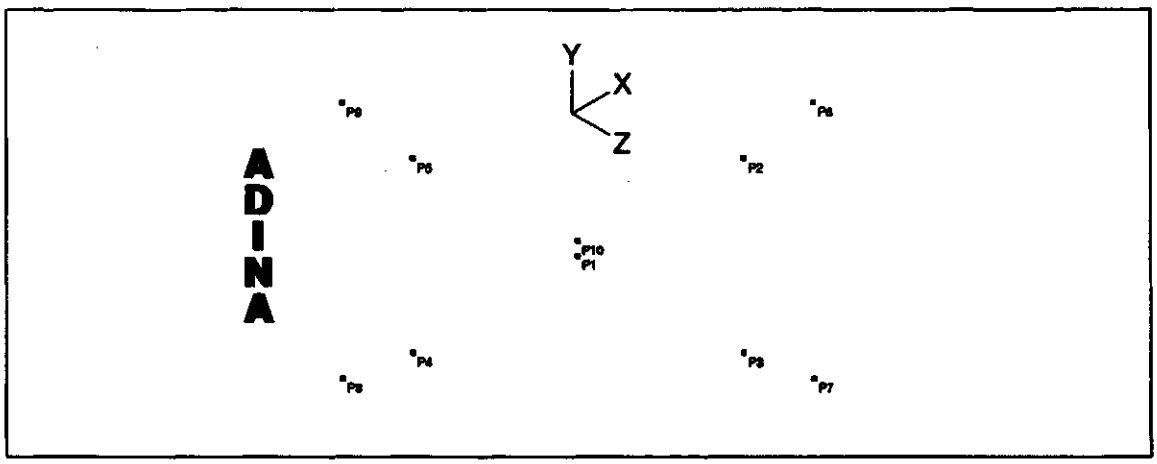

Figure 3.6: Lower Sheet Points.

Points P_2, P_3, P_4 and P_5 lie on the inner circumference with P_1 being the center of the inner circle (radius r_1), while points P_6, P_7, P_8 and P_9 are on the outer circumference with P_{10} being the center of the outer circle (radius r_2). Similarly, points from 11 to 20 define the upper sheet. The cylindrical copper mass will be

defined later as a body using the remaining two points and two of the predefined points. Figure 3.7 shows the geometry points of the sensor from three different views (Y-Z view, X-Y view and X-Z view).

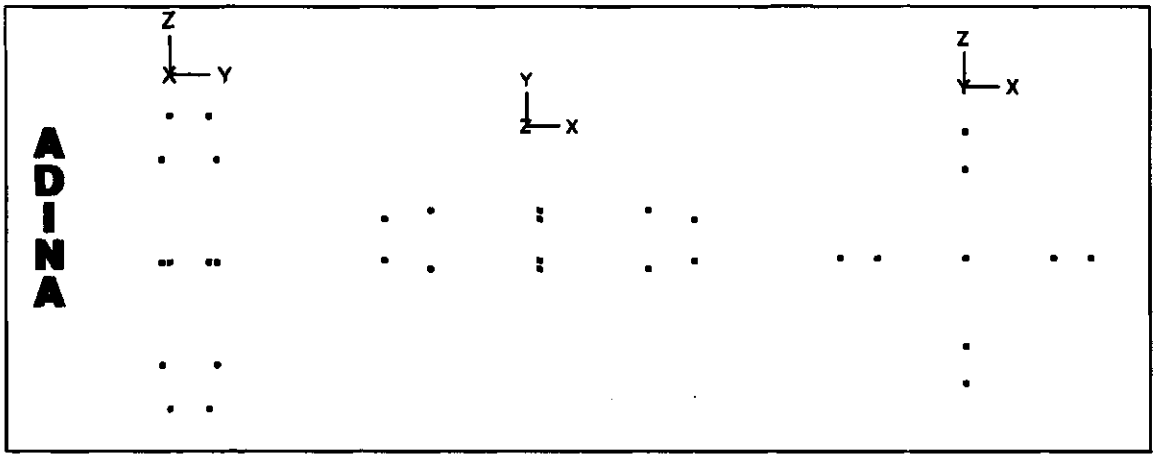

Figure 3.7: Three Different Views for Sensor Points.

Defining Geometry lines

ADINA connects two endpoints to form a geometry line which can be straight or curved. Lines are assigned unique numbers to label them as shown in Figure 3.8.

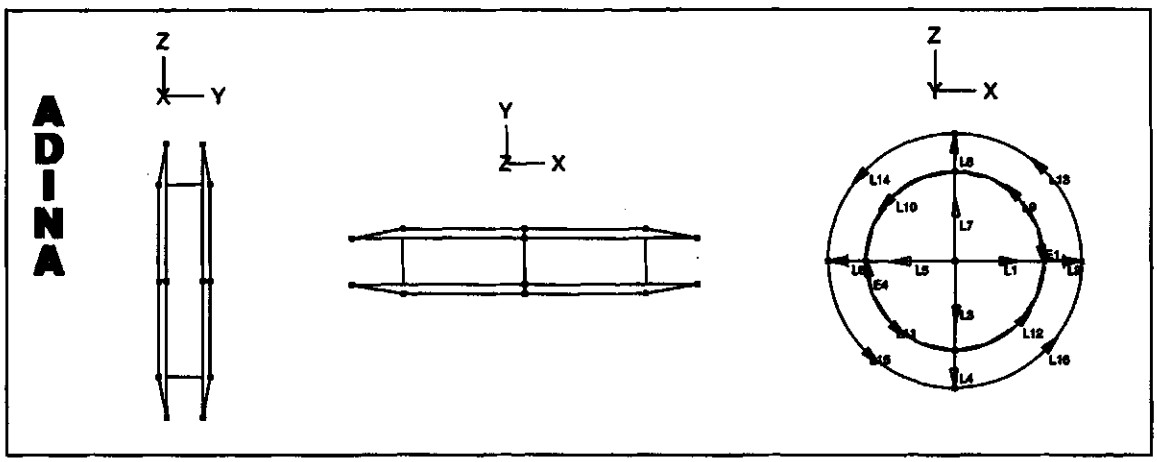

Figure 3.8: Sensor Lines.

Lines from 1 to 16 define the lower sheet. For simplicity, the model was designed in such a way that the diagonal lines lie on the X and Z axes as shown in the X-Z plane of Figure 3.8. Lines from 17 to 32 define the upper sheet.

Defining Geometry Surfaces

Surfaces can be flat or curved. Each surface has a type depending on how it is defined (by edge or by vertex). Patch type surfaces are defined by specifying the label numbers of geometry lines, which are the edges of the surface. The edge lines must form a connected sequence, i.e., their end points match. In vertex type, surfaces are defined by specifying the four vertices of the surface as geometry points. ADINA offers other types of surface definition such as grid, revolved, extruded and transformed surface, but were not used in this study. Each geometry surface is also assigned a number to label the surface.

The upper and lower sheets are divided into 8 surfaces each, four inner and four outer surfaces totalling 16 surfaces for the 2 piezo-film sheets in the sensor. Figure 3.9 shows the inner and outer surfaces of the upper sheet of the sensor, while the lower sheet is almost hidden.

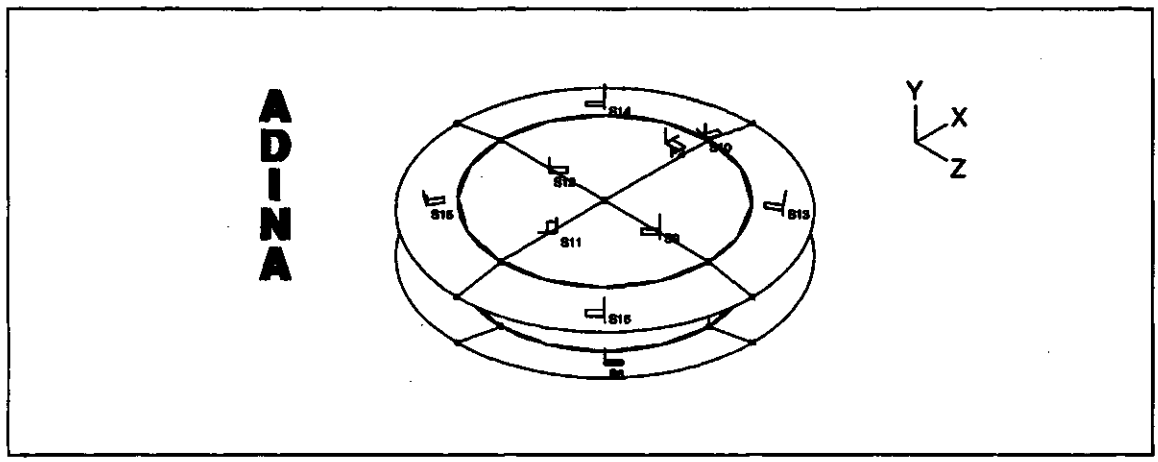

Figure 3.9: Sensor Surfaces.

Additional feature in surfaces is the ability to assign thickness to geometry surfaces, to be used when generating plate or shell elements on the surfaces. As the piezo-films have a thickness of 110 μm, this thickness had to be assigned to the 16 surfaces of the 2 piezo-film sheets.

Defining Geometry Volumes and Bodies

ADINA provides only four shapes for volumes, which are hexahedron, prism, tetrahedron and pyramid. Unfortunately none of these is applicable to the copper mass which is cylindrical. Hence the use of bodies was essential.

Geometry bodies are defined through ADINA-M (ADINA Modeler which uses the parasolid software as a CAD kernel to provide solid modelling capabilities). ADINA-M consists of a number of solid bodies for example block, cone, cylinder, pipe, prism and sphere. Figure 3.10 shows the cylindrical mass defined as body. The cylinder is defined by its center, length and radius. ADINA automatically generates the appropriate faces, edges and points needed for the cylinder. It also assigns a unique number for the body, the faces, the edges and the points generated.

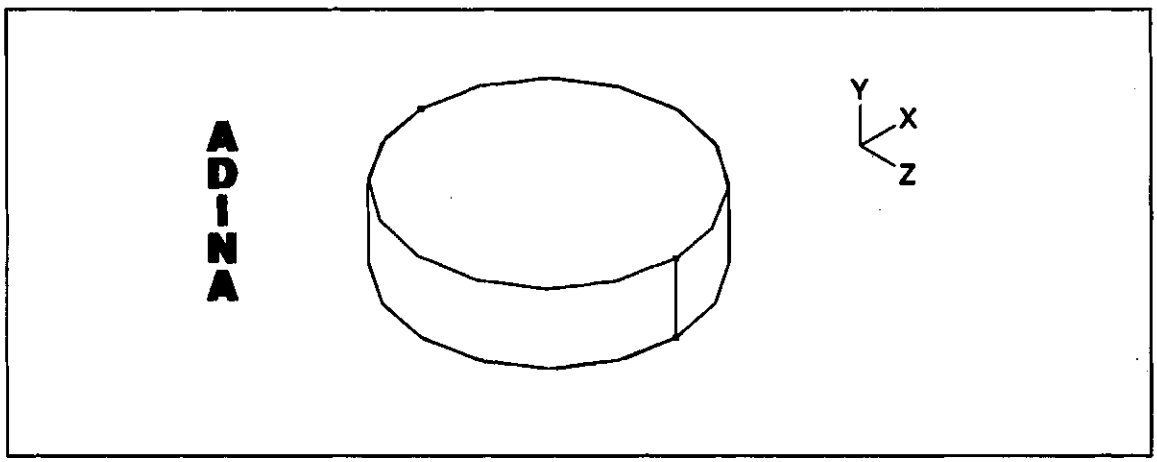

Figure 3.10: Copper Mass.

3.5.2 Material Description

A number is assigned to each material in the model. This number is unique for each material. The material can be assigned to an element group (this is then the default material for the element group) or to elements within an element group. All of the elements in an element group must reference materials of the same type. There are many material descriptions in ADINA. Most of these materials are for the analysis of solids e.g, elastic materials, plastic materials, rubber like materials and more.

The sensor has two materials with the following properties that has to be defined in the model.

Material 1 : Piezo-film with

1. Young's modulus = 4×10^9 N/m^2,
2. Poisson's ratio = 0.3,
3. Mass density = 1.78×10^3 Kg/m^3.

Material 2 : Copper Mass with

1. Young's modulus = 128×10^9 N/m^2,
2. Poisson's ratio = 0.36,
3. Mass density = 9.6619×10^3 Kg/m^3.

3.5.3 Boundary Conditions

Fixities are used to specify that certain degrees of freedom (DOF) have zero value. DOF are in x, y or z-translation and x, y or z-rotation. Fixities are defined in two

steps. In the first step, a fixity is defined independently of location where it is applied, and a name is assigned to it. In the second step the fixity is applied using its name to a location in the model. Fixities can be applied on nodes, lines, surfaces, edges, faces and/or bodies.

For the piezo-film sensor, two fixities are applied, denoted by B and C as shown in Figure 3.11. Suffixes 1, 2, and 3 in the figure indicate x, y and z directions respectively, while U and θ represent translation and rotation respectively. The first fixity, is on the 4 inner surfaces of the upper and lower sheets (surfaces 1, 2, 3, 4 of the lower sheet, and surfaces 9, 10, 11, 12 of the upper sheet in Figure 3.9), and they are fixed in all directions except the Y-translation represented by a check mark at U_2, denoting the translation in Y-direction. Second fixity is on the outer circumference of the sheets (lines 13, 14, 15, 16 on the lower sheet in Figure 3.8, and lines 21, 22, 23, 24 on upper sheet) denoted by C. These lines are totally fixed (i.e., no translations or rotations are allowed) so that these lines act as clamps simulating the top and bottom sheets in the actual structure.

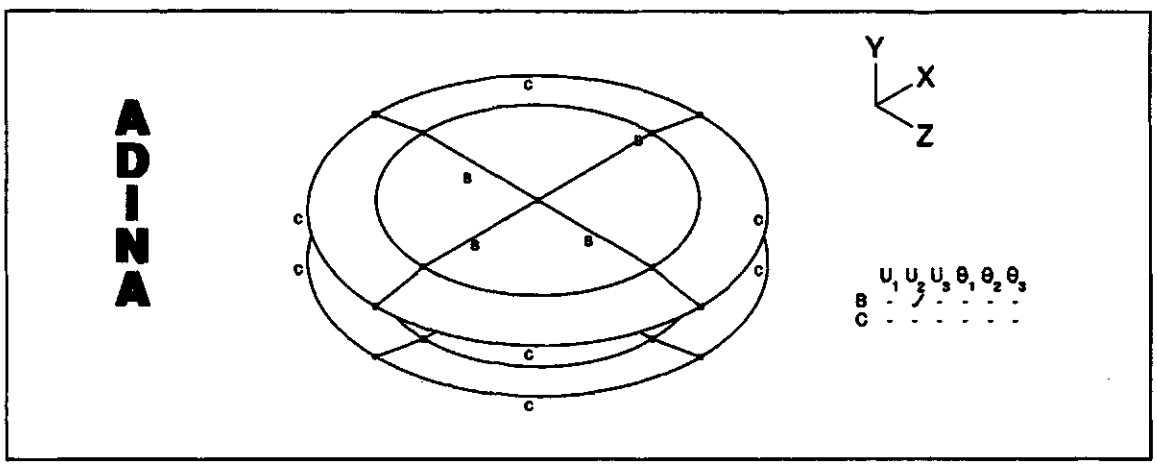

Figure 3.11: Boundary Conditions.

3.6 Defining Mesh Data

It has been indicated by Petyt [27] that, "the mesh size affects the accuracy of the results which means that it should be chosen to ensure that the quantities of interest are predicted accurately". There are two types of mesh elements, triangular and quadrilateral elements. Quadrilateral elements are usually used in preference to triangular elements as they tend to give more accurate results for the same arrangement of node points. Triangular elements are only used where the structural shape requires it.

3.6.1 Element Groups

Before defining elements, element groups containing those elements should be defined first. The element group specifies the type of element, the material type (from the material number assigned before), and other control information for the group. The following types of elements can be used in an ADINA analysis: truss, 2-D solid, 3-D solid, beam, plate, shell, pipe, and spring.

The sensor requires 2 element groups. One for the 2 piezo-film sheets and one for the copper mass. Choosing a shell element for the first group and 3-D solid for the second group seemed the most appropriate choice in designing the model.

3.6.2 Meshing Geometries

In order to mesh the geometry, subdivision data must be assigned to the geometry, then elements and nodes are generated on the geometry.

Subdivision Data

The subdivision data indicates the number and spacing of elements along the lines. This is done either by assigning the length of the element or simply assigning the number of subdivisions needed. For example, a line might have four equally spaced divisions along its length, which means that, during the meshing process, four elements will be placed onto the line. On a mesh plot that includes geometry lines, subdivision lines are plotted as small lines perpendicular to the geometry lines as shown in Figure 3.12.

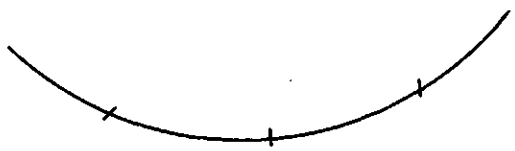

Figure 3.12: Subdivision.

Subdivision is achieved either through lines and edges or through surfaces, volumes, faces and bodies or through the entire model.

When subdividing through surfaces, volumes, faces or bodies, subdivision data for the surface, volume, face or body is specified and the program passes the subdivision data to each of the attached lines or edges.

When subdividing the entire model, subdivision data for the entire model is specified and the program passes the subdivision data to each of the lines of the model.

Two meshing techniques were used to assign subdivisions for the sensor. For the piezo-film sheets, all lines are assigned three subdivisions as shown in Figure 3.13.

To investigate the effect of refining the mesh, the number of subdivisions is increased as will be discussed in the next chapter. Generally, each line can have a different number of subdivisions. The second technique used was subdividing the

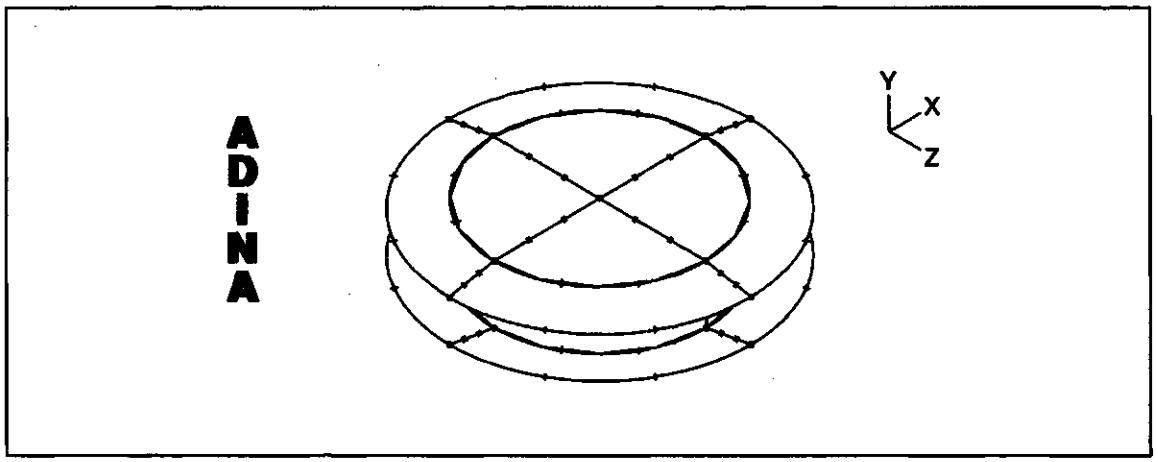

Figure 3.13: F.E Mesh Density for Piezo-Film Sheets with All Lines Assigned 3 Subdivisions.

body, for the cylindrical copper mass, and the program passes the subdivision data to each of the attached lines or edges within the body. Assigning 3 subdivisions, automatically subdivides each line in the body to three equal subdivisions as shown in Figure 3.14.

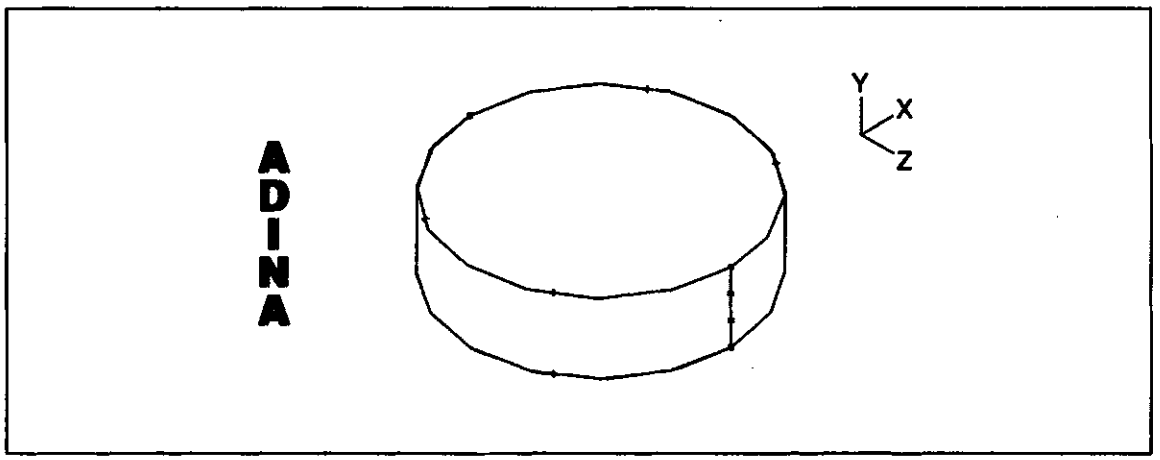

Figure 3.14: F.E Mesh Density for Copper Mass Body (With 3 Subdivisions).

Mesh Creation

In the process of generating the elements, element groups should be chosen to include those new generated elements. If the geometry primitive has data corresponding to the type of element selected with the element group, the program applies this property data to each generated element. The actual number and placement of the elements is determined by the mesh generation algorithms.

For point mesh algorithm, ADINA places a node at a geometry point. For line or edge mesh, the number and spacing of the created elements is determined by the subdivision data given for the line or the edge. For the surface or volume mesh, the program uses the subdivision data for the bounding lines to determine the number and the spacing of the elements. The mesh generation algorithm divides the surface or volume into quadrilateral and/or triangular cells, each of which is then filled with an element or several elements. For face or body the subdivision data for the bounding edges is used to determine the number and spacing of the created elements.

For the sensor model, surface mesh for the 2 piezo-film sheets was selected, where ADINA uses the 3 subdivisions assigned for the bounding lines to determine the number and spacing of the created shell elements. In this case ADINA generated 120 shell elements for the 2 piezo-film sheets. For the copper mass cylinder, body mesh was selected, again ADINA uses the assigned subdivisions (which are 3 subdivisions) for the bounding edges to determine the number and spacing of the generated 3D solid elements, which were found to be 101 3D solid elements.

A report, which ADINA automatically generated, for the model information with the 3 subdivisions was as follows:

143 nodes.

2 element groups:

Element group 1: 120 shell elements.

Element group 2: 101 3D solid elements.

221 elements total.

Figure 3.15 shows the created mesh for the sensor using surface mesh for the piezo-film sheets and body mesh for the copper mass.

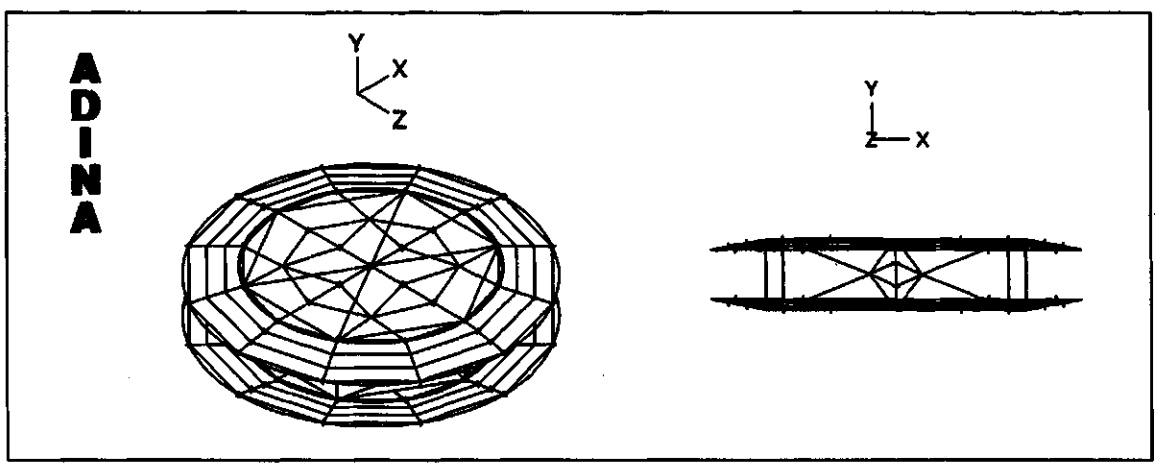

Figure 3.15: F.E Sensor Mesh with the 3 Subdivisions.

3.7 Loads

In ADINA, loads are also defined in 2 steps, first the load is defined independent of the location where it is to be applied and a number is assigned to it. The second step is applying the load, using its number, to a location in the model. Loads are applied either to points, lines, edges, surfaces, volumes or bodies. There are many different types of loads. For ADINA, types as force, moment, displacement, pressure, line, centrifugal, mass proportional, electromagnetic, temperature and temperature

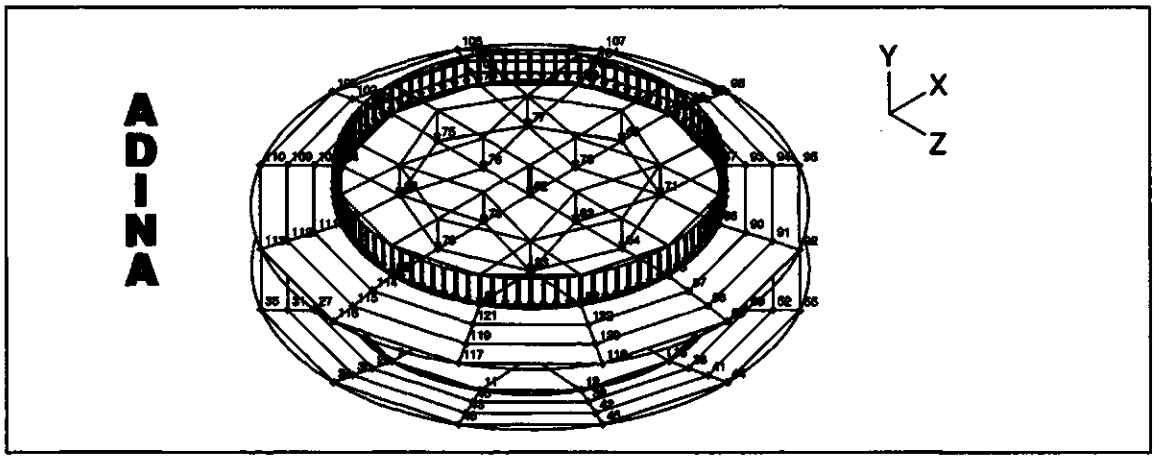

Figure 3.16: Applied Load.

gradient are allowed. In ADINA, by default the load is constant over the line, surface, or volume, unless otherwise specified.

For this study, pressure was the type of load applied on the 4 inner surfaces of the upper sheet (S_9, S_{10}, S_{11}, and S_{12} shown in Figure 3.9). The pressure load is distributed on the generated nodes, as shown in Figure 3.16, which shows how the load is applied on the sensor.

3.8 Generating the Solution Program Input Data File

Once the model definition is completed, an input data file for the solution program has to be generated. While generating the input data file, ADINA displays a window called "Log window" with information from the input file generation. If there are errors in the model definition, ADINA will not create an input data file (and will not overwrite any existing input data file). ADINA writes the error messages into the Log window.

4. FINITE ELEMENT ANALYSIS AND RESULTS

4.1 Types of Analysis

In this chapter different analyses are applied to the proposed FE model in ADINA and their results are compared to the experimental and theoretical results.

ADINA provides different types of analysis such as:

1. static analysis,

2. frequency analysis,

3. mode superposition dynamic analysis,

4. modal stress calculation,

5. calculation of modal participation factors and other quantities used in response spectrum, random or harmonic vibration analysis,

6. transient dynamic analysis or in other words direct time integration dynamic analysis,

7. linearized buckling analysis, and,

8. collapse analysis, which is static analysis.

In the following sections, further discussion will be presented for the types of analysis that were used in this study.

The next phase was validating the FE model developed earlier. This is achieved by comparing some of the numerical results from the FE model with the theoretical results.

4.2 Frequency Analysis

All systems possessing mass and elasticity are capable of free vibration (which is the vibration occuring after an impulse). The analysis of a structure in free motion provides the most important dynamic properties of the structure, which are the natural frequencies and the corresponding modal shapes. Mode shapes are useful because they represent the shape that the structure will vibrate in free motion. Refer to Appendix A for the first three natural frequencies and their corresponding mode shapes of a simply supported beam.

A system consisting of a single mass and a single linear spring is considered to be a single degree of freedom system, where there is only one mode shape at a specific frequency (natural frequency), whereas dealing with a FE structure, there is more than one degree of freedom (multiple degree of freedom). For a multiple degree of freedom system with N degrees of freedom, N mode shapes and N natural frequencies will exist. Each mode has a natural frequency associated with it. Generally, the first mode of vibration is the one of primary interest. The first mode occurs at the lowest (first) natural frequency of a system. Higher order modes also exist for a structure, but they occur at higher natural frequencies. In this study, only the first mode shape of the piezo-film sensor and its corresponding natural frequency are considered.

Figure 4.1 shows on the left the FE model of the piezo-film sensor, developed in Chapter 3, with its first mode shape on the right and its corresponding natural frequency.

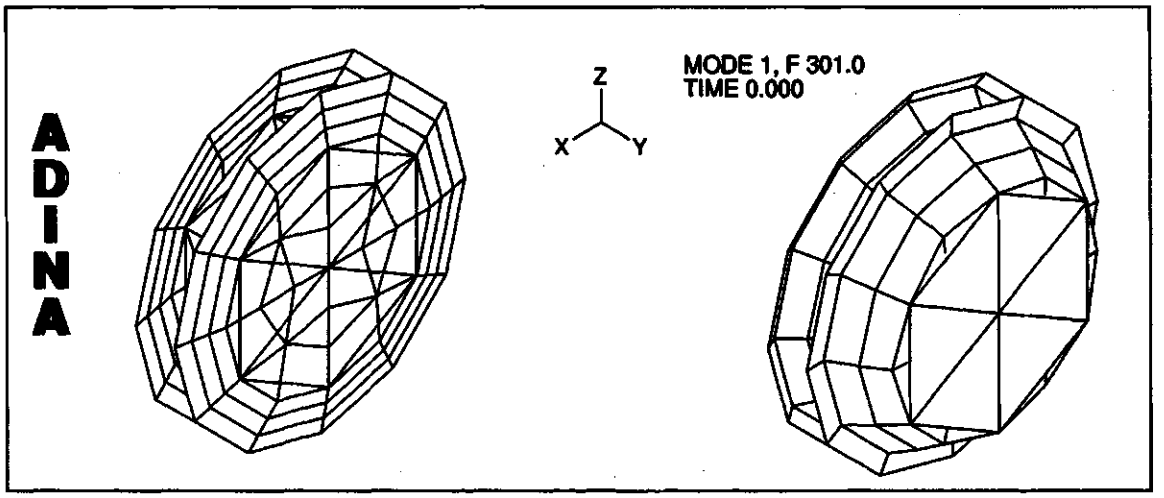

Figure 4.1: FE Model of the Sensor and its First Mode Shape with 3 Subdivisions.

4.2.1 Mesh Refinement

As mentioned in the previous chapter, it is necessary to refine the mesh and compare results from both solutions (refined and unrefined meshes) to reassure accuracy.

It was found that increasing the number of subdivisions for all the lines in the piezo-film sheets and for the copper mass, decreased the natural frequency, approaching the theoretical natural frequency of the system.

Table 4.1 summarizes, the number of subdivisions assigned to the copper mass cylinder and to the two piezo-film sheets, information about the model giving the number of nodes created according to the subdivision technique chosen, the number of shell elements created for the piezo-film sheets, the number of the 3D solid elements created for the copper mass and finally, the result from the frequency analysis, which is the natural frequency for each case.

Figure 4.2 shows the last mesh refinement applied to the FE sensor model in which, five subdivisions were assigned to all lines of the piezo-film sheets and 5 subdivisions

Table 4.1: Summary of F.E Model of Sensor.

No. of Copper Mass Subdivisions	No. of Sheets Subdivisions	No. of Model Nodes	No.of Shell Elements	No.of 3D Solid Elements	Natural Frequency (Hz)
3	3	139	120	83	301
4	4	302	224	271	284.7
5	5	425	344	307	277.6

for the copper mass.

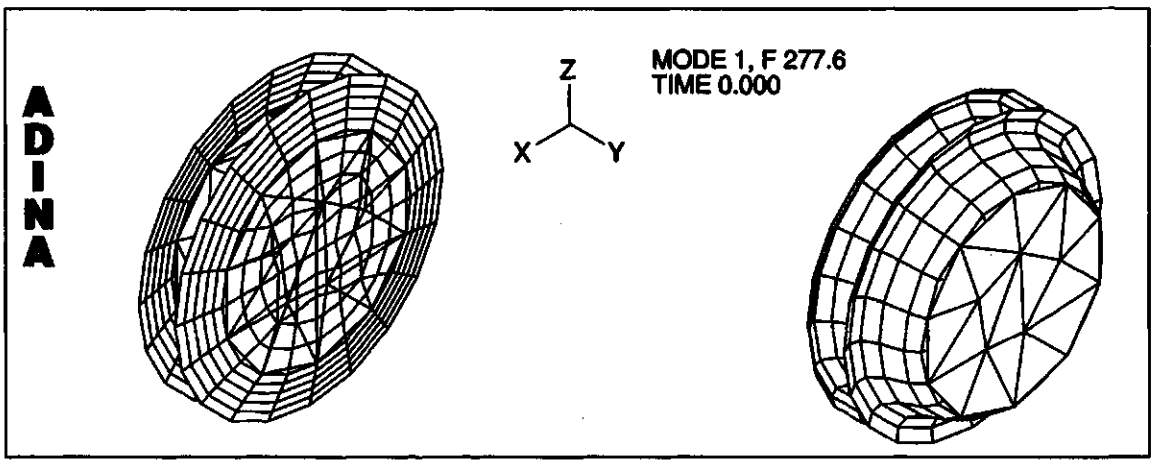

Figure 4.2: FE Model of the Sensor and its First Mode Shape with 5 Subdivisions.

As for the piezo-film sheets, the region between radius r_1 and radius r_2 acts as a spring, it is considered to be the most effective part. Accordingly, the number of subdivisions assigned for this region was doubled (10 subdivisions) to increase the accuracy of the results. The model information report generated by ADINA, for the sensor with 10 subdivisions in the region between radii r_1 and r_2 while keeping the rest with 5 subdivisions as before, was as follows:

625 nodes.

2 element groups:

Element group 1: 544 shell elements.

Element group 2: 307 3D solid elements.

851 elements total.

Figure 4.3 shows three different views of the sensor model, assigning 10 subdivisions to the lines connecting the inner circumference to the outer one, with natural frequency being 277.1 Hz.

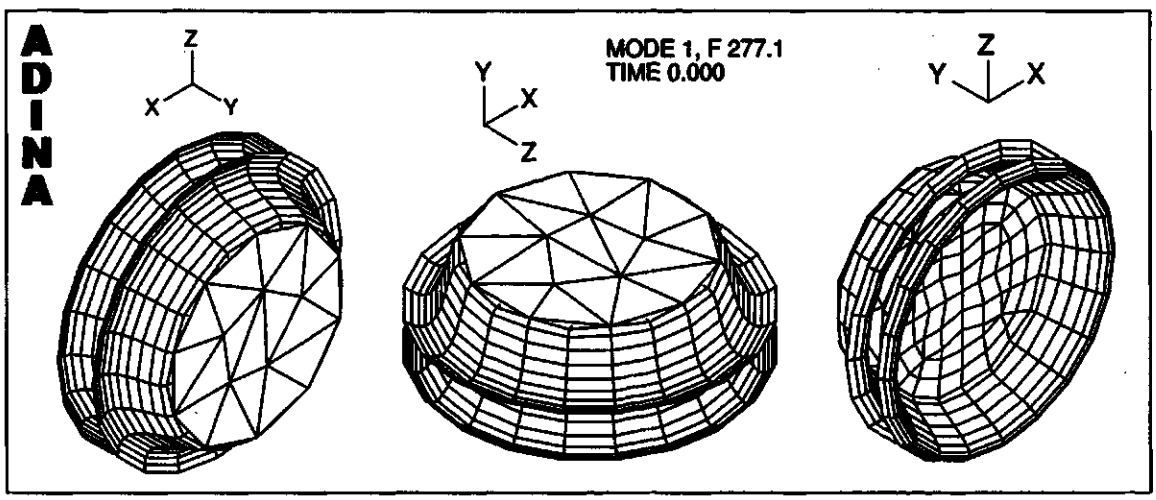

Figure 4.3: Different Views for the Sensor with 10 Subdivisions in the Region Between Radii r_1 and r_2.

Table 4.2 shows a comparison between the theoretical natural frequency of the sensor from Chapter 2 and the numerical natural frequency from the finite element simulation. The deviation from the theoretical value was tabulated for all cases studied. Also Table 4.2 shows how the use of a finer mesh improves the results. A percentage difference of about 4 % between the theoretical and numerical value (last

Table 4.2: Comparison Between Theoretical and FE Results for the Natural Frequency of the Sensor.

	Natural Frequency (Hz)	Deviation from Theoretical
Theoretical	266.03 [17]	-
F.E 3 Divs	301	13.14 %
F.E 4 Divs	284.7	7.01 %
F.E 5 Divs	277.6	4.35 %
F.E 10 Divs	277.1	4.16 %

case) confirms the validity of the FE model.

4.3 Static Analysis

A static analysis calculates the effects of steady loading conditions on a structure, while ignoring inertia and damping effects, such as those caused by time-varying loads. The static analysis is used to determine the displacements, stresses, strains, and forces in structures subjected to a steady load. The kinds of loading that can be applied in a static analysis include: externally applied forces and pressures.

As the input acceleration used experimentally was 0.5 m/s^2, hence the pressure used was calculated via Equation (4.1).

$$P = \frac{F}{A_p} = \frac{m \times acc}{\pi \times r_1^2}, \tag{4.1}$$

where m is the mass of the copper cylinder, acc is the input acceleration, and A_p is the surface area on which the pressure is to be applied.

Figure 4.4 shows how a static pressure load (N/m^2) is applied to the upper sheet.

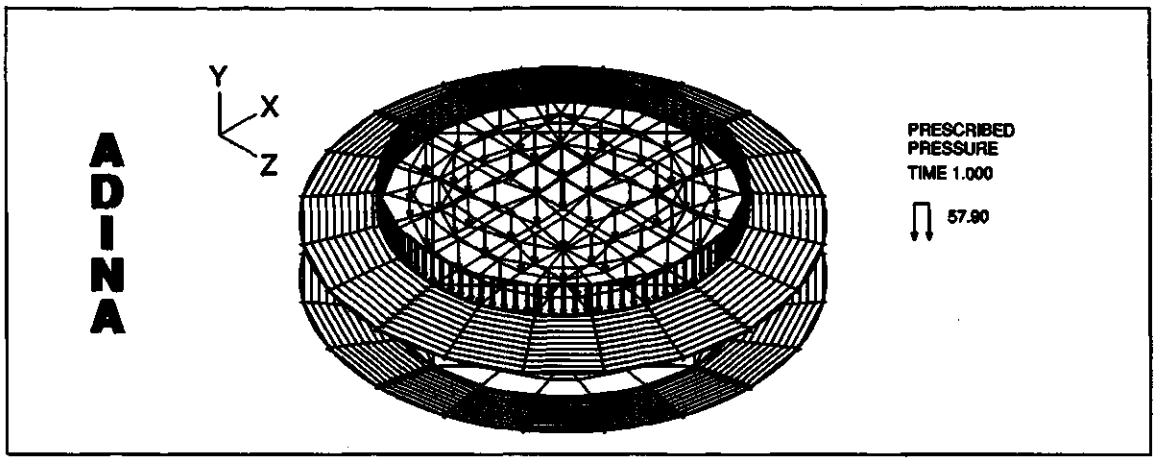

Figure 4.4: Application of a Static Load of 57.9 N/m^2 on the FE Model of the Sensor.

The pressure load is distributed and applied on all the generated nodes of the upper sheet. The effect of this pressure load on the FE model of the sensor is shown in Figure 4.5.

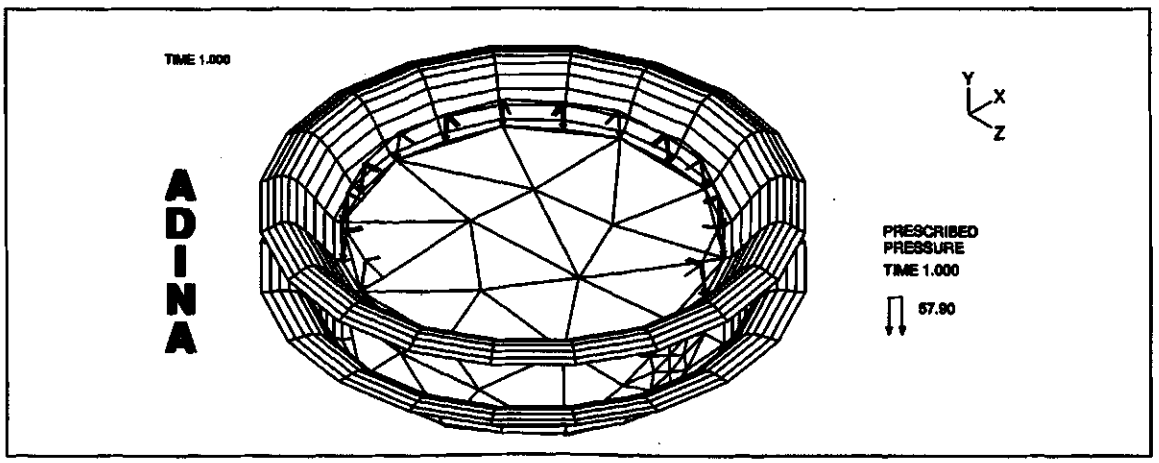

Figure 4.5: Effect of Static Pressure Load of 57.9 N/m^2 on the FE Model of the Sensor.

Considering the region from the center to the outer circumference of the upper

sheet. The line chosen was a diagonal lying on the z axis, on which nodes were generated. The stress in the three directions (x, y and z) together with the resultant stress for each node were plotted in ADINA-PLOT against the distance as shown in Figure 4.6 for the upper sheet, where the resultant stress is defined as,

$$\sqrt{(STRESS_{XX})^2 + (STRESS_{YY})^2 + (STRESS_{ZZ})^2}.$$

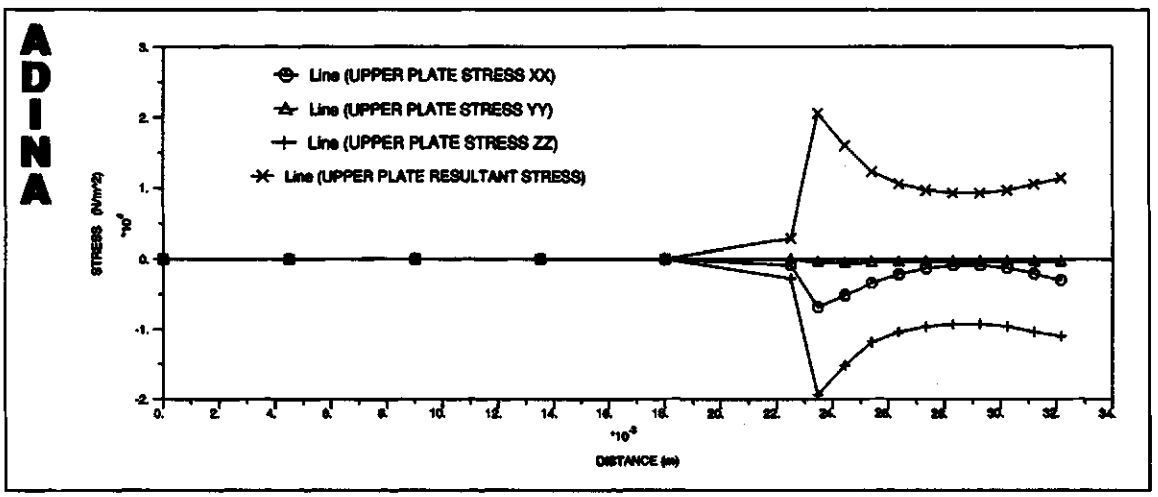

Figure 4.6: Effect of Applying a Static Pressure Load of 57.9 N/m^2 on the Upper Sheet.

The curve indicates that there is relatively small stress from the center of the sheets, then it increases due to the tension on the region from r_1 to r_2. From r_1 the stress decreases due to the fact that $T = F/A$ where $A = 2\pi rh$, i.e., as the radius increases, the stress decreases. But it starts to increase again near the boundary due to the clamping of the edge, where h is the thickness of the piezo-film sheet.

4.4 Transient Analysis

Transient dynamic analysis (sometimes called time-history analysis) is a technique used to determine the dynamic response of a structure under the action of any general

time-dependent loads. This type of analysis is used to determine the time-varying displacements, strains, stresses, and forces in a structure as it responds to any combination of static, transient, and harmonic loads. The time scale of the loading is such that the inertia or damping effects are considered to be important. Damping dissipates energy and causes the amplitude of free vibration to decay with time.

In Chapter 2, Equation (2.5) for a single degree of freedom was studied, but dealing with a finite element structure, for which there is more than one degree of freedom, x_δ is replaced by a vector D of nodal degrees of freedom and $m\gamma(t)$ is replaced by a load vector R, which may contain moments as well as forces and which is a known function of time. Also, k, c, and m are, respectively, replaced by a stiffness matrix K, a damping matrix C, and a mass matrix M. Thus the equation analogous to Equation (2.5) for a multi-degree of freedom structure is

$$KD + C\dot{D} + M\ddot{D} = R, \tag{4.2}$$

where R = R(t). This is the governing equation of structural dynamics, written in its most common form, it states that externally applied forces R are resisted by the sum of three internal forces: stiffness forces KD, damping forces $C\dot{D}$, and inertia forces $M\ddot{D}$ [27–29, 31]. The following sections present the damping analysis in the considered system.

4.4.1 Half Power Bandwidth Method

The half-power bandwidth method is used to estimate the damping ratio from the frequency domain (using the experimental curve). Corresponding to each natural frequency, there is a peak in frequency response amplitude, 3 dB (which is $max/\sqrt{2}$) down from the peak there are two points corresponding to half power points. Figure 4.7 shows these 2 points on the experimental curve.

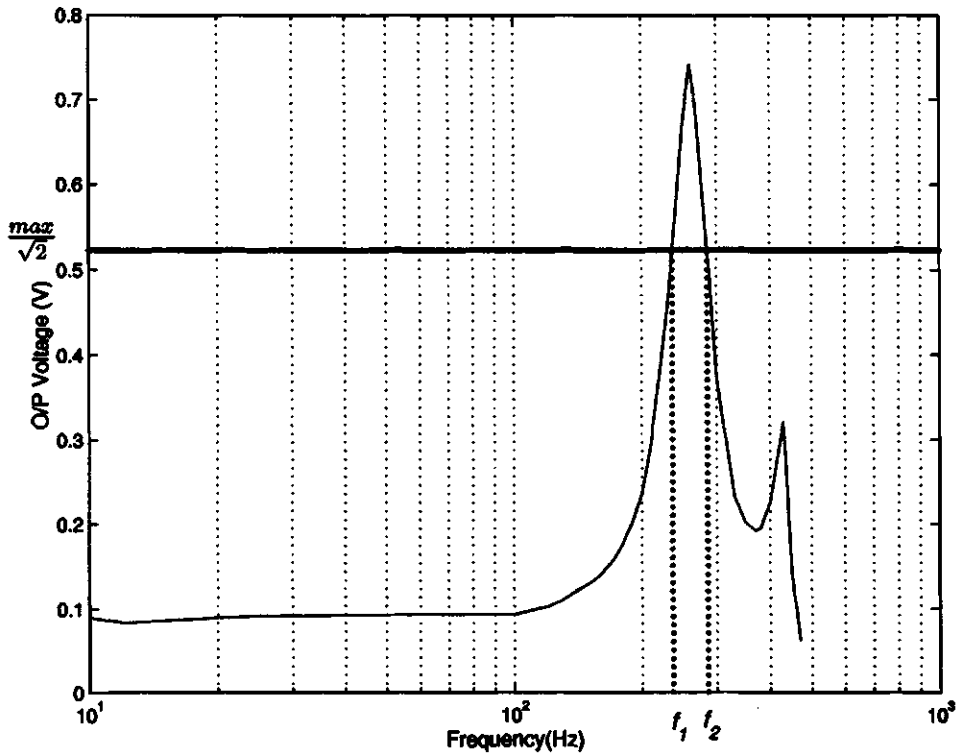

Figure 4.7: Half Power Bandwidth Method.

The damping ratio is defined as the ratio of the frequency range between the two half power points to twice the natural frequency at the same mode [32–34].

$$\zeta = \frac{f_2 - f_1}{2f_n}. \tag{4.3}$$

Using the experimental curve in Figure 4.7 and Equation 4.3, the experimental damping ratio was found to be $\zeta_{exp} \approx 0.09$.

4.4.2 Rayleigh Damping

The damping ratio of a system is included in FE analysis via Rayleigh damping. Rayleigh damping refers to the following definition of the damping matrix: [27–29,31]

$$C = \alpha M + \beta K. \tag{4.4}$$

The values of α and β are not generally known directly, but are calculated from the damping ratio, ζ_i, for a particular mode of vibration, i. If ω_i is the natural circular frequency of mode i, then α and β will satisfy the relation

$$\zeta_i = \frac{\alpha}{2\omega_i} + \frac{\beta\omega_i}{2}. \tag{4.5}$$

To specify both α and β for a given damping ratio ζ, (which is chosen according to the experimental results), it is commonly assumed that the sum of the α and β terms is nearly constant over a range of frequencies. Therefore, given ζ and a frequency range ω_i to ω_j, α and β can be calculated via

$$\beta = \frac{2(\zeta_j\omega_j - \zeta_i\omega_i)}{\omega_j^2 - \omega_i^2}, \tag{4.6}$$

$$\alpha = 2\omega_i\zeta_i - \beta\omega_i^2. \tag{4.7}$$

But applying the calculated constants α and β (corresponding to the experimental damping ratio calculated previously from Equation 4.3) to the FE model, the peak obtained was much lower than the experimental one, which means that a lower damping ratio is needed for this model to give the same frequency response as the experimental one (N.B. the damping ratio only affects the peak).

According to this, the damping ratio had to be adjusted in such a way to give the same response, and the chosen value was $\zeta = 0.04$, which is less than the experimental damping ratio due to unaccounted frictional loss in the FE model. A suitable frequency range $\omega_1 < \omega_n < \omega_2$ is chosen, and a graph showing the damping ratio versus the frequency curve is shown in Figure 4.8.

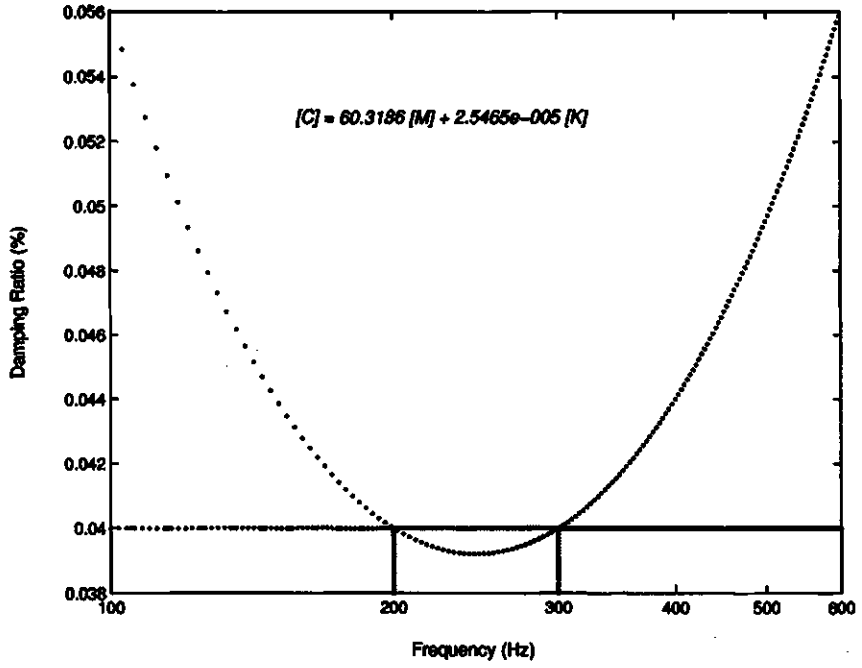

Figure 4.8: Rayleigh Damping Ratio Versus Frequency Curve.

4.4.3 Experiment Simulation on ADINA

To simulate the experiment, that was done in the lab on the actual sensor, using the data acquisition system [6], a sinusoidal pressure load

$$P = P_o cos(\omega t) \tag{4.8}$$

with $P_o = 57.9$ N/m^2 (equivalent to the input acceleration of 0.5 m/s^2 with varying frequency in the experiment) was applied to the sensor model in ADINA.

The input frequency is varied (from 10 Hz to 500 Hz), and with each frequency, the ADINA transient analysis is run, in which step by step direct integration is applied. Stress in the three different directions on the upper and lower piezo-film sheets was investigated, specifically the area between radii r_1 and r_2, that's why the subdivision in this particular part was doubled; to increase the number of nodal points between them as already mentioned.

Starting at frequency 10 Hz and increasing the frequency gradually until reaching the natural frequency of the system and exceeding it, reaching a frequency of 500 Hz, calculation of the resultant stress for both sheets was done by ADINA.

(i) Stresses At Middle Point

Considering the point in the midway between r_1 and r_2, and plotting the three stress components obtained from the step by step direct integration at different frequencies. It was found that for lower frequencies, 10 Hz to 100 Hz, there is a transient which dies down rapidly. Then a steady-state sinusoidal response which decays very slowly with time as the sensor has a low damping ratio as shown in Figure 4.9.

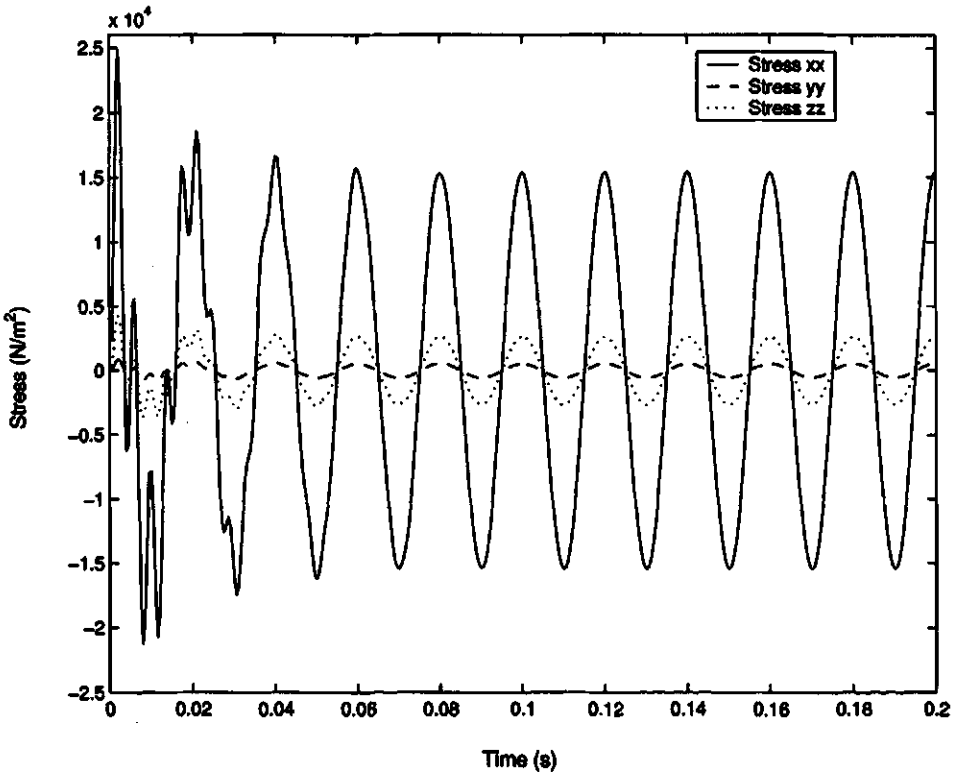

Figure 4.9: Stresses at Middle Point (Between r_1 and r_2) of Lower Sheet at Low Frequency (50 Hz).

As for higher frequencies (close to the natural frequency), Figure 4.10 shows a plot of the stresses in the x, y and z directions versus time. There is no transient part, but the steady-state sinusoidal response is achieved in less time.

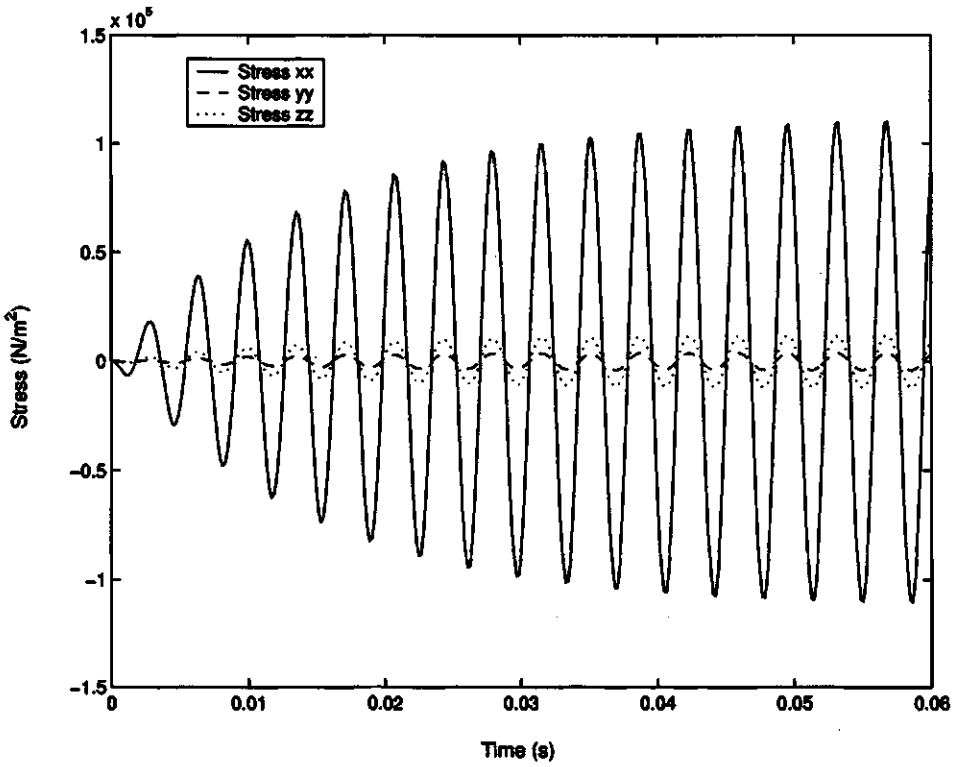

Figure 4.10: Stresses at Middle Point (Between r_1 and r_2) of Upper Sheet at High Frequency (277 Hz).

(ii) Variation Of Output Stress With Frequency

For each frequency, the resultant output stress,

$$\sqrt{(Stress_{xx})^2 + (Stress_{yy})^2 + (Stress_{zz})^2},$$

where Stress_{xx} is the stress in x-direction, Stress_{yy} is the stress in y-direction and Stress_{zz} is the stress in z-direction for the nodal points on a line from the center of

the sheets to the clamped part is calculated (the line considered lies on the x-axis from the center to r_1 then the line joining r_1 to r_2).

Considering each nodal point of the 11 points from r_1 to r_2 for the 2 sheets, the maximum stress at each frequency, in the range of frequency required, is obtained. For each frequency, the average resultant stress from the 11 nodal points is calculated and plotted. A plot of stress versus frequency for both the upper and lower sheets is shown in Figure 4.11.

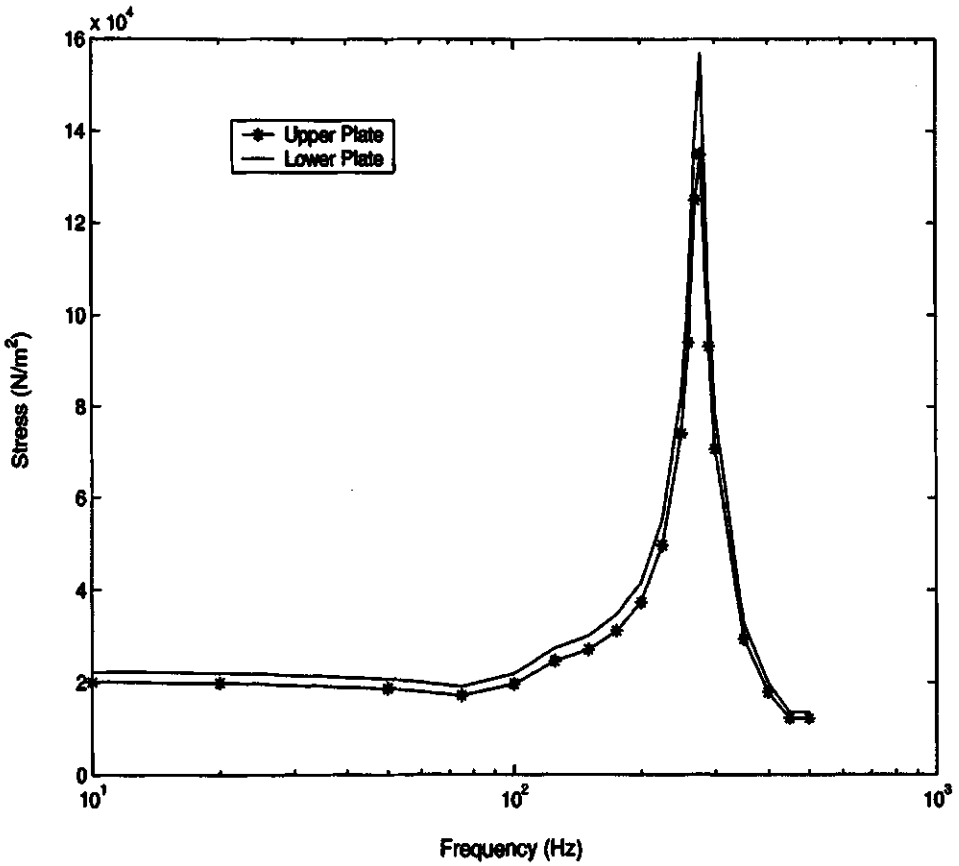

Figure 4.11: FE Results of Output Stress Versus Frequency for Both the Lower and Upper Sheets.

(iii) Comparison Between Experimental, Theoretical, and Numerical Results.

Calculating the average output stress from both sheets for each frequency, the line curve in Figure 4.12 is obtained which represents output stress against frequency for the sensor. The dash-dot curve represents the experimental lab results, while the dotted curve represents the theoretical Simulink results. There is a close resemblance between the three results, while keeping in mind that the output voltage of the sensor is proportional to the average output stress from the sheets.

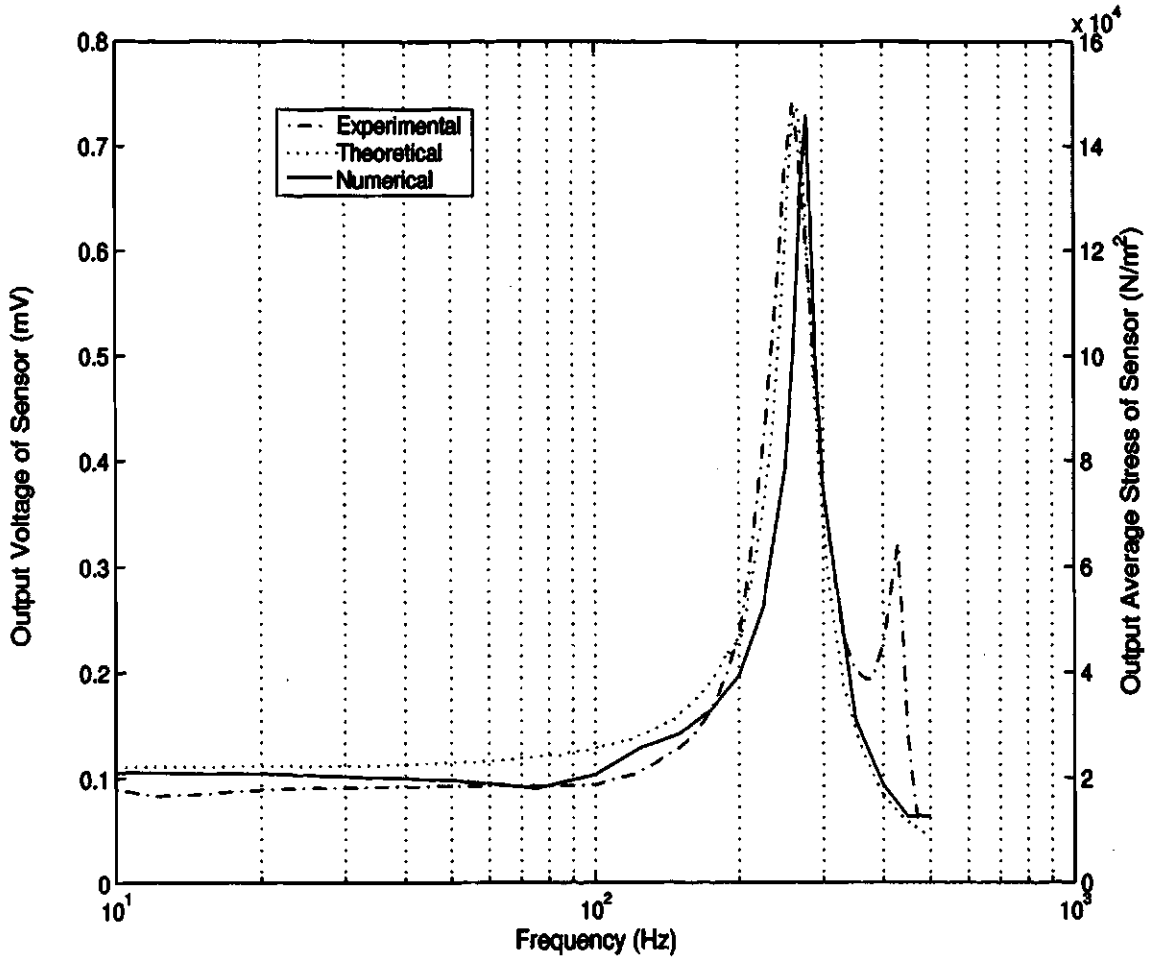

Figure 4.12: Comparison between Experimental, Theoretical and Numerical Results.

The finite element result shows that in the frequency range from 10 to 100 Hz, the output stress was constant, resembling the experimental and theoretical results which had constant O/P voltage in the same frequency range.

4.5 Use of Finite Element Results

Liu et al [13] state that "the basic FE method, for piezoelectric accelerometer modelling, is used purely for mechanical analysis, e.g. to determine the natural frequencies, resonance modes, stresses and other parameters". In the previous sections, the natural frequency of the system was determined which was comparable to the theoretical natural frequency. Also the frequency response of the FE sensor model resembled the curves from the experimental and analytical analysis.

Based on the simulated model, other parameters are considered. The yield strength of a material is an important issue which should be considered to ensure non breakage of the sheets.

Again considering the diagonal line from the center to r_2, the stress for the points near the center is relatively very small, increasing gradually till the stress reaches the maximum at about 0.023 m (at the first node after r_1) , then the stress decreases gradually until approaching the edge at r_2 where it starts to increase again due to the clamps as shown for the upper sheet at frequency 50 Hz in Figure 4.13.

Figure 4.14 shows the stress on the upper and lower sheets at a certain time where there is a peak (i.e., maximum stress) at 277 Hz frequency. The curves shown in Figures 4.13 and 4.14 clearly indicate that the highest stress occurs at around 0.023 m from the center for the upper sheet. Also it is shown that frequencies near the natural

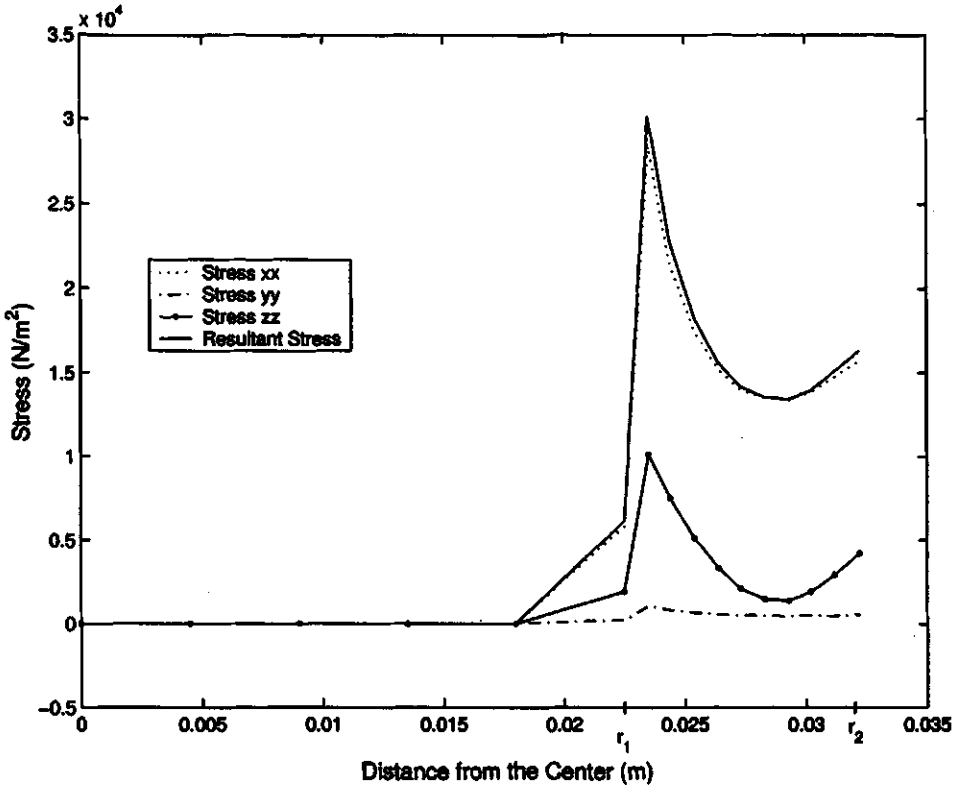

Figure 4.13: Upper Sheet Stress at Frequency 50 Hz.

frequency undergo the highest stress (about 2.5× 10^5 N/m^2) on the piezo-film sheets which is still far from the yield strength of the PVDF material (45-55 × 10^6 N/m^2).

4.5.1 Changing Design Parameters

Since the finite element model can be altered relatively easily, hence the finite element method of structural analysis enables the designer to detect stresses, and vibration problems during the design process and to evaluate the results due to specific changes before the construction of a prototype. Thus confidence in the acceptability of the prototype is enhanced. Moreover, if used properly, the method can reduce the number of prototypes that need to be built. The parameters changed in this study

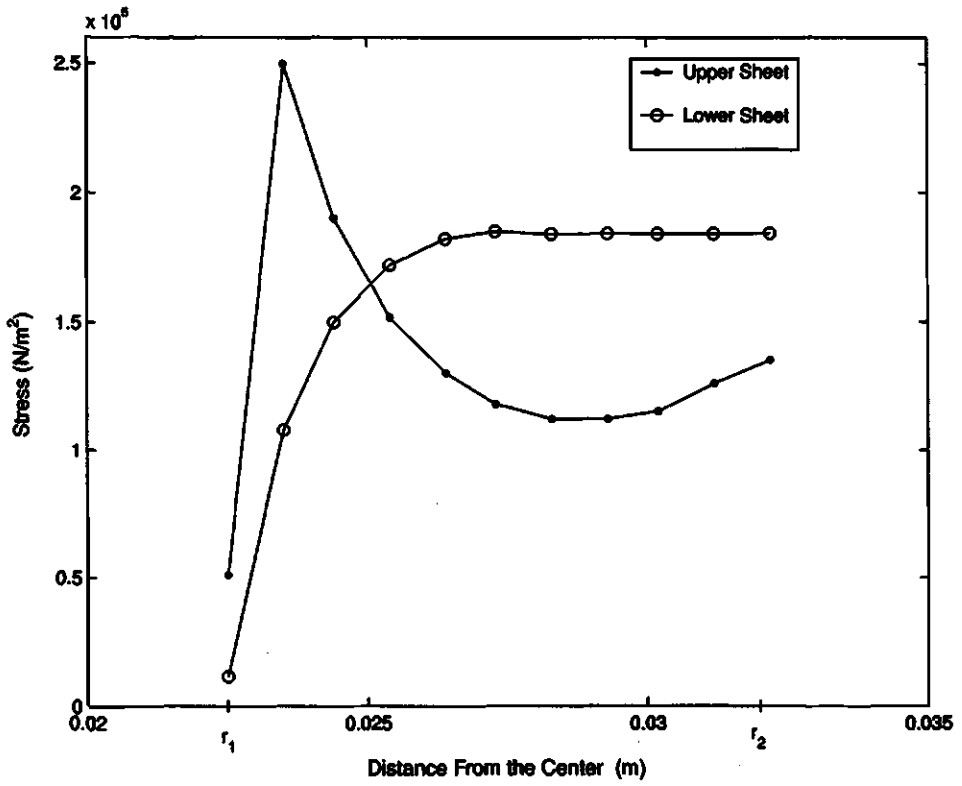

Figure 4.14: Resultant Stress of Upper and Lower Sheets at Frequency 277 Hz.

were, the thickness of the sheets (h) and their outer radii (r_2). Also, the design changes considered analytically in Chapter 2 were applied to the designed finite element model of the sensor producing similar results (which were halving both radii and changing the mass distance above the plexiglass structure).

The first change considered in Chapter 2 was reducing both radii (r_1) and (r_2) of the piezo-film sheets by half, maintaining the same copper mass. Figure 4.15 shows the first mode shape of such sensor with its corresponding natural frequency (494.5 Hz) using the finite element model. The theoretical natural frequency from Chapter 2 was about 507 Hz, giving a percentage difference from the numerical results of about 2.5 %.

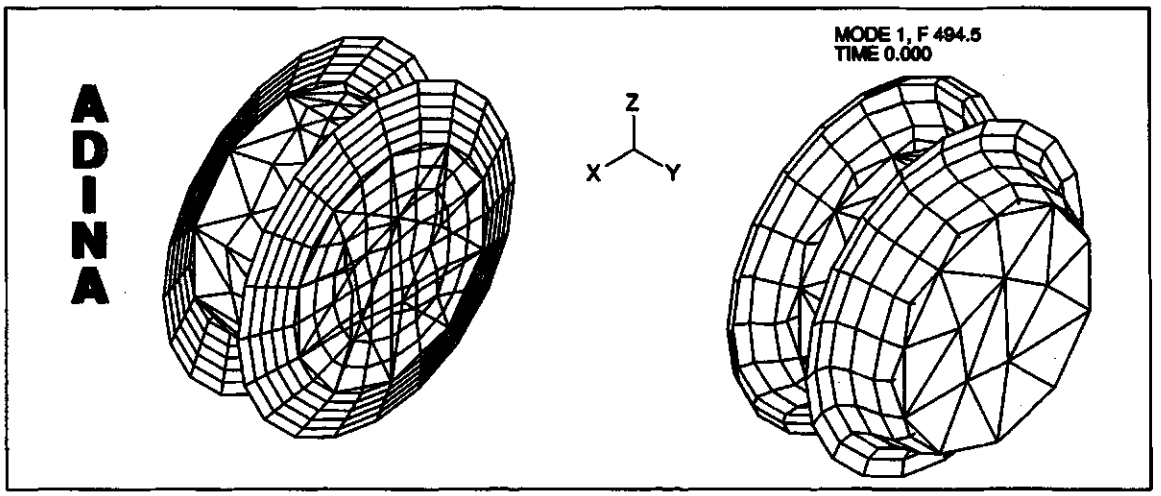

Figure 4.15: First Mode Shape of the Sensor and its Natural Frequency with Both Radii Being Halved.

The second change discussed in Chapter 2 was doubling the distance x_d which in the FE model is the vertical distance between the clamps and the mass (Figure 2.3 in Chapter 2). This was also checked numerically via the FE model. Figure 4.16 shows the first mode shape and the natural frequency of such design of the sensor. The natural frequency being 490.8 Hz, giving a percentage difference of about 3 % from the theoretical natural frequency which was 507 Hz.

Change Sheets' Thickness

Using the FE simulated model, the thickness of the 2 piezo-film sheets was changed. The first thickness assigned was 13.75 μm, then it was increased gradually by doubling the thickness each time until a thickness of 880 μm is reached. Frequency analysis is performed on each model for the different thicknesses assigned. The natural frequency of the sensor corresponding to each thickness is obtained and plotted. As indicated by the line curve in Figure 4.17, increasing the thickness of the piezo-film

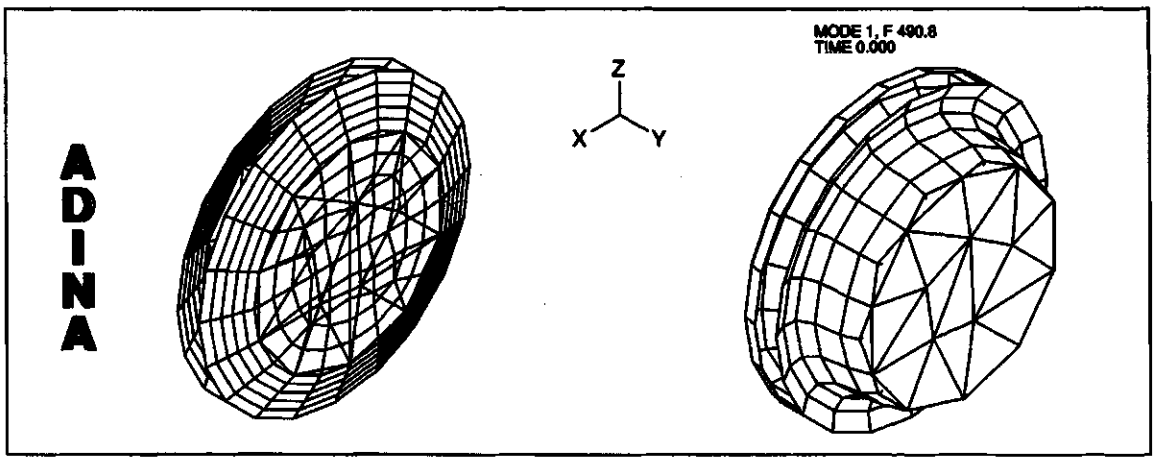

Figure 4.16: Effect of Doubling the Distance x_d on the Natural Frequency of the Sensor and its First Mode Shape.

sheets, increases the natural frequency of the system.

This result agrees with the theoretical view. Equation (2.8) in Chapter 2 together with Equation (2.4), indicate that, the spring constant, k, is proportional to the thickness as follows,

$$k = \lambda h, \tag{4.9}$$

where, λ equals,

$$\frac{4\pi Y \sin^2 \phi}{\ln\left(\frac{r_2}{r_1}\right)}$$

where h is the thickness of the piezo-film sheets. Also it is known that, the natural frequency of the spring f_n is defined in terms of k by

$$f_n = \frac{1}{2\pi}\sqrt{\frac{k}{m}} \tag{4.10}$$

Hence, from Equations (4.9 and 4.10), it is proved analytically that the natural frequency is proportional to square root of the thickness of the piezo-film sheets, which is plotted as the dash-dot curve in Figure 4.17. The point marked with a circle

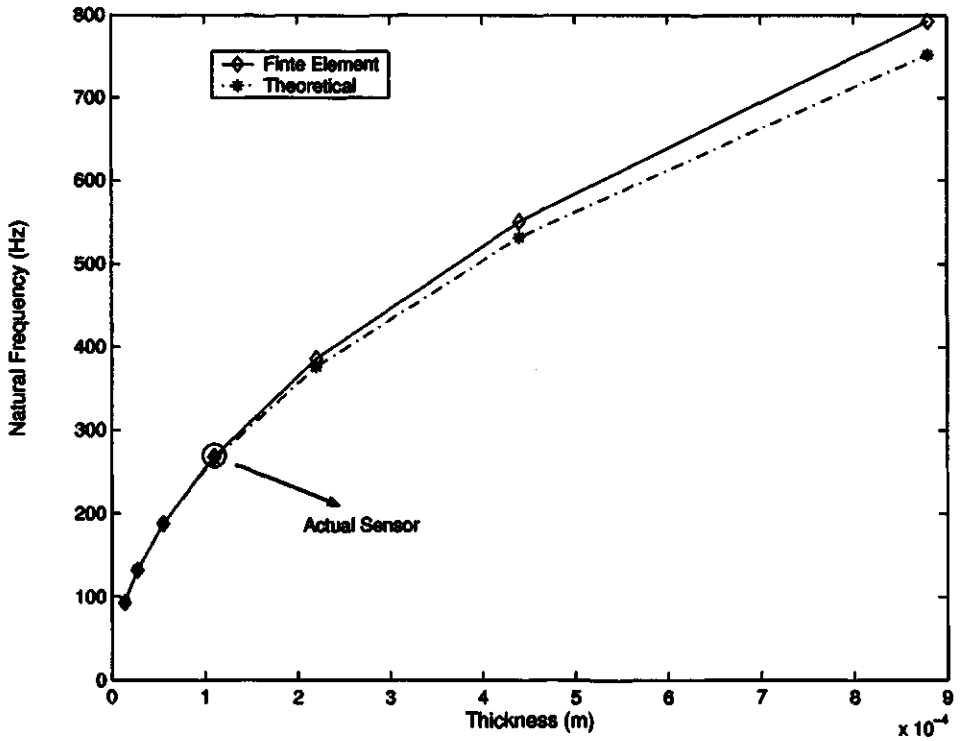

Figure 4.17: Effect of Changing Thickness of Piezo-Film Sheets on the Natural Frequency of the Sensor.

is the thickness of the actual sensor (110 μm).

Change Sensor Outer Radius

In this section, the effect of altering the outer radius while maintaining the same inner radius of $r_1 = 0.0225$ m is studied. The outer radius started at 0.024875 m and was increased gradually by an increment of $\frac{(r_2 - r_1)}{8}$. Figure 4.18 shows the effect of varying the outer radius of the piezo-film sheets on the natural frequency of the system.

Considering Equation (2.8) in Chapter 2, it implies that increasing the distance

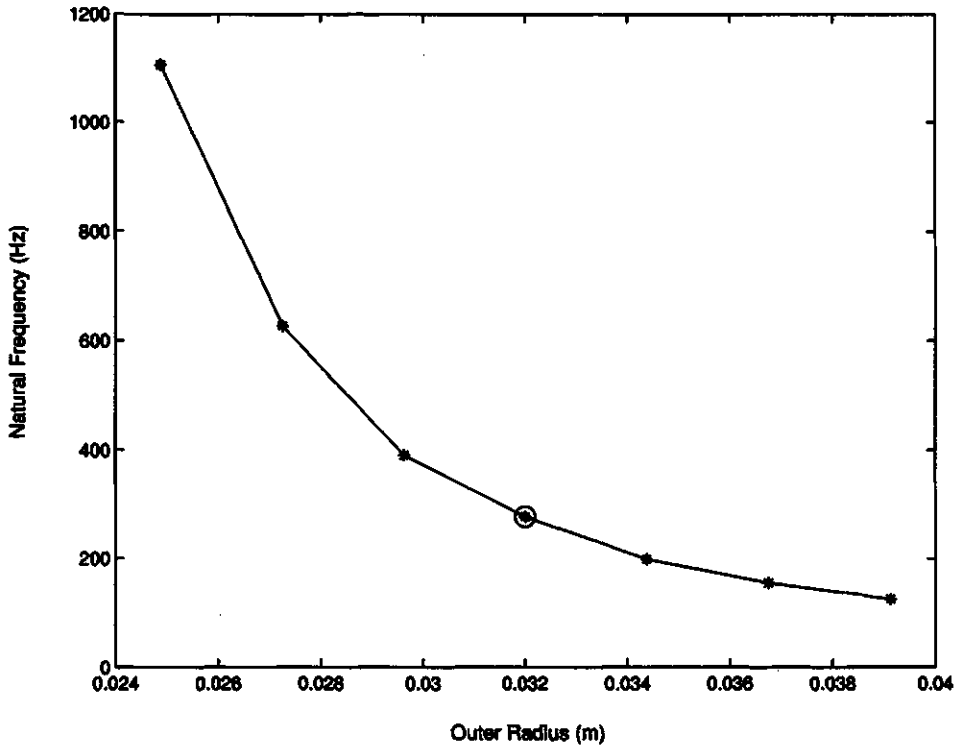

Figure 4.18: Effect of Changing Outer Radius of the Sensor on its Natural Frequency.

between r_1 and r_2 decreases the stiffness constant k_ϕ which consequently decreases the natural frequency of the system. Again the point with circle mark is the one representing the actual sensor.

5. SUMMARY AND CONCLUSIONS

The intent of this research was to develop a finite element model for a piezo-film acceleration transducer for low frequency vibration monitoring. A validated finite element model of a transducer makes it possible to predict its behavior if some design parameters are changed. Vibration monitoring sensors can be used in a wide range of operating frequencies, and finite element simulation can evaluate different designs to suit the needed frequency, before actually building the sensor.

Generally piezoelectric accelerometers have been modelled using analytical methods. Chapter 2 presents the basic construction of the considered sensor, a derivation of the theoretical model for the piezo-film sensor based on electromechanical analogy. It was then simulated using Simulink. The theoretical results were compared to the experimental lab results validating the mathematical model. This chapter serves as a background for the development of the finite element model to understand the sensors' construction and behavior.

The goals achieved in this study were:

1. A finite element model for the considered sensor was developed in ADINA software, which is a powerful software tool for dynamic structural finite element simulations.

2. The finite element model was validated by comparing its numerical results with the theoretical results. It was found that the natural frequency from both results were almost the same with a percentage difference of 4 %, which is acceptable. Also its

first mode shape was plotted.

3. The effect of increasing the number of nodes (using finer mesh) was also investigated. It indicated that increasing the number of nodes and elements created enhances the accuracy of the results. But there is a limit on mesh refinement depending on the availability of the computer power.

4. The experiment done in the lab (via the data acquisition system) was simulated by the validated finite element model. The curve from the numerical results represented the output stress on the piezo-film sheets which is proportional to the output voltage from the experimental and theoretical results. The output from the three results (experimental, theoretical and numerical) was constant in the frequency range from 10 to 100 Hz, which is the bandwidth of the system.

5. Also, the maximum stress exerted on the piezo-film sheets was investigated, to ensure non breakage of the system. When the sensor was subjected to an acceleration of 0.5 m/s^2, it was found that the maximum stress exerted on the sheets is less than 1 % of the yield strength of the piezo film material.

6. Finally, some design parameters were changed, and the effect of these changes was studied. For instance, increasing the thickness of the piezo-film sheets increased the natural frequency of the system. While increasing the outer radius of the piezo-film sheets, decreased the systems' natural frequency. Also, it was found that reducing the size of both sheets by half, maintaining the same copper mass, or doubling the vertical distance between the clamps and the copper mass, doubled the natural frequency of the system.

5.1 Future Work

There are several recommendations for future work. One of which is, reducing the size of the sensor by decreasing the sheets' size and/or decreasing the mass of the copper cylinder. By diminishing the sensor size, it can be used in fine applications such as biomedical ones or applications needing tiny sensors.

Another one is simulating the electrical characteristics of the piezoelectric accelerometers, which remains a challenging task, optimizing the electric sensitivities as a function of frequency, while keeping the resonance frequency as high as possible using the FE method.

Also changing the materials' properties used in the sensor, studying the effect of several materials on its behavior, and optimizing it before making actual prototypes, according to the applications' needs can be done with the aid of a FE model.

References

[1] Fukada E. and Furukawa T., "Piezoelectricity and ferroelectricity in polyvinylidene fluoride," *Ultrasonics*, pp. 31–39, January 1981.

[2] Kepler R.G. and Anderson R.A., "Ferroelectric polymers," *Advances in Phys*, vol. 41, pp. 1–57, 1992.

[3] Broadhurst M.G., Davis G.T., and Mckinney J.E., "Piezoelectricity and pyroelectricity in polyvinylidene fluoride-a model," *J. Appl. Phys.*, vol. 49, no. 10, pp. 4992–4997, October 1978.

[4] Thompson M.L., "On the material properties and constitutive equations of piezoelectric poly vinylidene fluoride(pvdf)," Ph.D. thesis, Drexel University, 2002.

[5] Measurement Specialties, *Peizofilm Sensors Technical Manual*, Measurement Specialties, Inc., 1999.

[6] Daku B.L.F. and Prugger A.F., "A microseismic piezofilm sensor," *IEEE Canadian Conference on Electrical and Computer Engineering*, pp. 483–487, May 2002.

[7] Jenq S.T. and Chang C.K., "Characterization of piezo-film sensors for direct vibration and impact measurements," *Experimental Mechanics*, vol. 35, pp. 224–232, September 1995.

[8] Han J.H., Rew K.H., and Lee I., "An experimental study of active vibration control of composite structures with a piezo-ceramic actuator and a piezo-film sensor," *Smart Mater. Struct.*, vol. 6, no. 5, pp. 549–558, 1997.

[9] Chen Q.X. and Payne P.A., "Industrial applications of piezoelectric polymer transducers," *Measurement Science and Technology*, vol. 6, pp. 249–267, 1995.

[10] Santamarina J.C., Wakim T.N., Tallina A.G., Rab F., and Wong J., "Piezo film technology and applications in geotechnical testing," *Geotechnical Testing Journal*, vol. 14, no. 4, pp. 363–370, December 1991.

[11] Benech P., Chamberod E., and Monllor C., "Acceleration measurement using pvdf," *IEEE Trans. Ultrasonics, Ferroelectrics and Frequency Control*, vol. 43, no. 5, pp. 838–843, September 1996.

[12] Brown R.H., "Piezo film: Form and function," *Sensors And Actuators A: Physical*, vol. 22, no. 1-3, pp. 729–733, 1990.

[13] Liu B. and Kreigbaum B., "Piezoelectric accelerometer modification based on the finite element method," *International Journal of Acoustics and Vibration*, vol. 5, no. 1, pp. 23–26, May 2000.

[14] Soderkvist J., "Using fea to treat piezoelectric low-frequency resonators," *IEEE Trans. Ultrasonics, Ferroelectrics and Frequency Control*, vol. 45, no. 3, pp. 815–823, 1998.

[15] Kekana M., "Finite element modelling of laminated piezo-elastic structures," *Journal of Sound and Vibration*, vol. 256, no. 3, pp. 463–473, 2002.

[16] Preumont A. Piefort V., "Finite element modelling of smart piezo-electric shell structures," *Fifth National Congress On Theoretical and Applied Mechanics*, May 2000.

[17] Daku B.L.F., Mohamed E., and Prugger A.F., "A pvdf transducer for low-frequency acceleration measurements," *Accepted by ISA Transactions*, 2004.

[18] Rajan J., "Portable wideband microseimic data acquisition system," M.Sc. thesis, Dept. of Electrical Engineering, University of Saskatchewan, Canada, 2000.

[19] Kraft M., "Closed loop digital accelerometer employing oversampling conversion," Ph.D. thesis, Coventry University, School of Engineering, UK, 1997.

[20] Brindley K., *Sensors and Transducers*, Heinemann Professional Publishing, 1988.

[21] Tierstein H.F., *Linear Piezoelectric Plate Vibration*, Plenum Press, New York, 1969.

[22] Berlincourt D.A., Curran D., and Jaffe H., "Piezoelectric and piezomagnetic materials and their function in transducers," in *Physical Acoustics, Principles and Methods*, W.P. Mason, Ed., New York, 1964, vol. 1, pp. 169–270.

[23] MathWorks, *Simulink 6.5 Release 13*, www.mathworks.com, 2002.

[24] Leung A.Y.T. Cheung Y.K., Lo S.H., *Finite Element Implementation*, Blackwell Scienc Ltd, 1996.

[25] Logan D.L., *A First Course in the Finite Element Method Using Algor*, Wadsworth Group, 2001.

[26] Norton H.N., *Handbook of Transducers*, Prentice Hall, 1989.

[27] Petyt M., *Introduction to Finite Element Vibration Analysis*, Cambridge University Press, 1990.

[28] Cook R.D., *Finite Element Modeling for Stress Analysis*, John Wiley And Sons Inc., 1995.

[29] Bathe K.J., *Finite Element Procedures*, Prentice Hall, 1996.

[30] On Line Manual, *ADINA System 8 Release Notes*, ADINA R & D, Inc., Sept 2002.

[31] Beards C.F., *Structural Vibration 'Analysis And Damping'*, John Wiley And Sons Inc., 1996.

[32] Nashif A.D., Jones D.I.G., and Henderson J. P., *Vibration Damping*, John Wiley & Sons, 1985.

[33] Shabana A.A., *Theory of vibration*, Springer-Verlag New York, Inc, 1991.

[34] Thompson W.T., *Theory of Vibration with Applications*, Prentice Hall, 1988.

A. APPENDIX A

Simple Example on ADINA: Natural Frequencies and Mode Shapes of a Simply Supported Beam.

A.1 Simply Supported Beam Example

In the following analysis, a finite element model using ADINA is presented. Natural frequencies are obtained and compared with the analytical results. The exact natural frequencies and mode shapes of a simply supported beam are given analytically in [31].

A simply supported steel bar with length, $L = 1.5$ m and a circular cross section with diameter, $D = 3$ cm as shown in Figure A.1 is modelled via ADINA as follows:

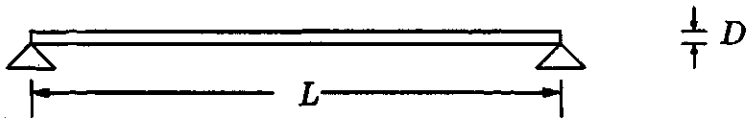

Figure A.1: Simply Supported Beam.

Figure A.2 shows the geometry points needed for the model.

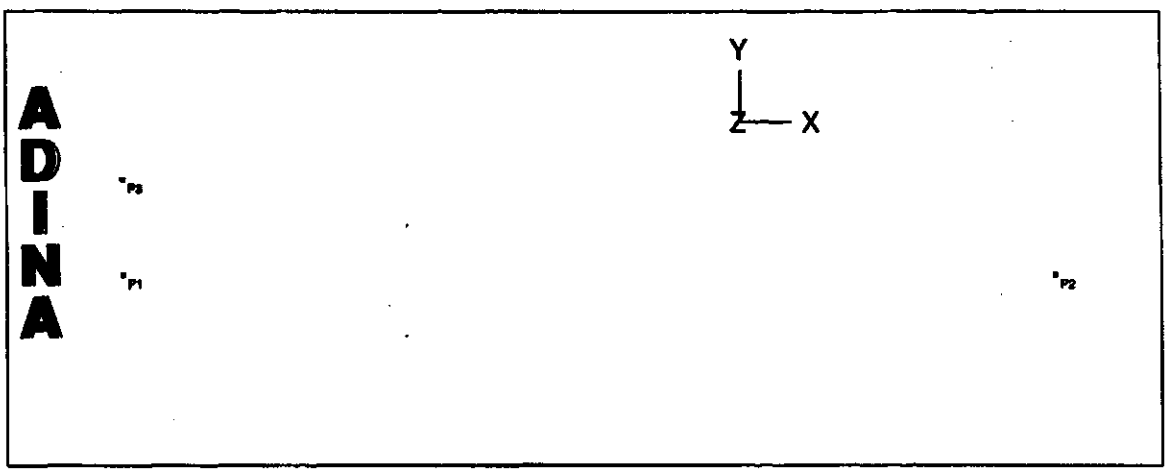

Figure A.2: Points of Beam.

A line connecting points P_1 and P_2 modelling the beam is constructed as shown

in Figure A.3. Point P_3 is an auxiliary point used only in case of beams, to define the directions of the element local coordinate system.

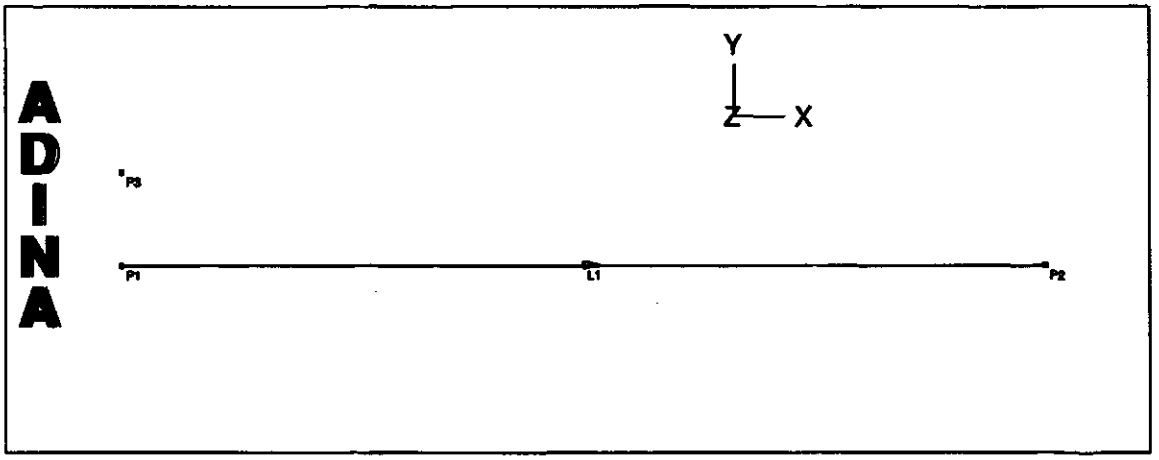

Figure A.3: Lines of Beam.

The cross section of the beam is then defined, also the properties of the material which are its density: 7780 Kg/m^3 and its Young's Modulus: 208×10^9 N/m^2 are defined.

The boundary conditions are then defined to model the simple support at both ends. Points P_1 and P_2 are marked B which denotes that they are only kept free in Z-Rotation (θ_3) as shown in Figure A.4. θ_1 and θ_2 are not shown as all nodes in the body were not allowed to rotate around X and Y through the "Master Degrees of Freedom" option.

The next step in developing a FE model is choosing a suitable element. In this case, the beam element is chosen.

The final step is meshing the model. The beam is divided into seven subdivisions as shown in Figure A.5. Then a mesh is created by choosing the mesh line option. The nodes created for the beam with 7 subdivisions are shown in Figure A.6.

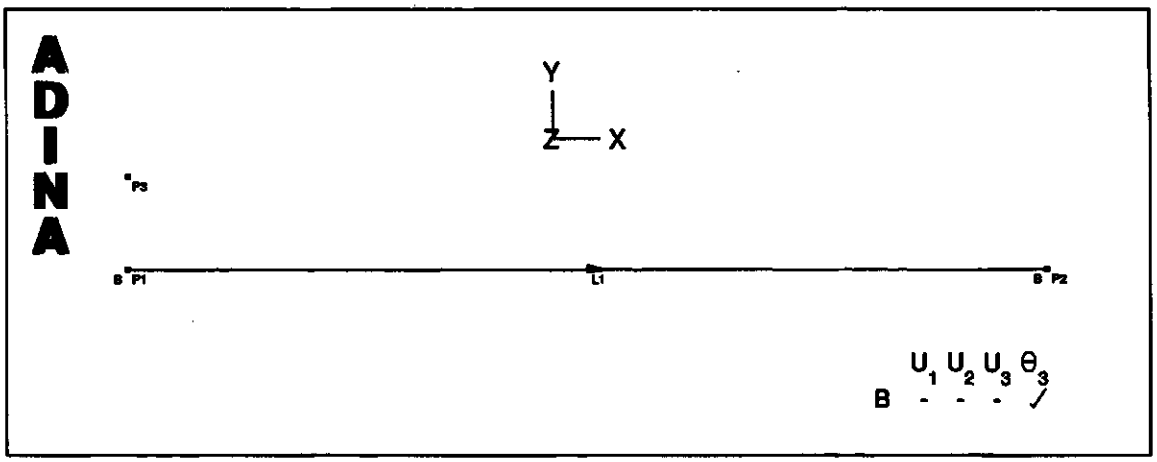

Figure A.4: Boundary Conditions on a Simply Supported Beam.

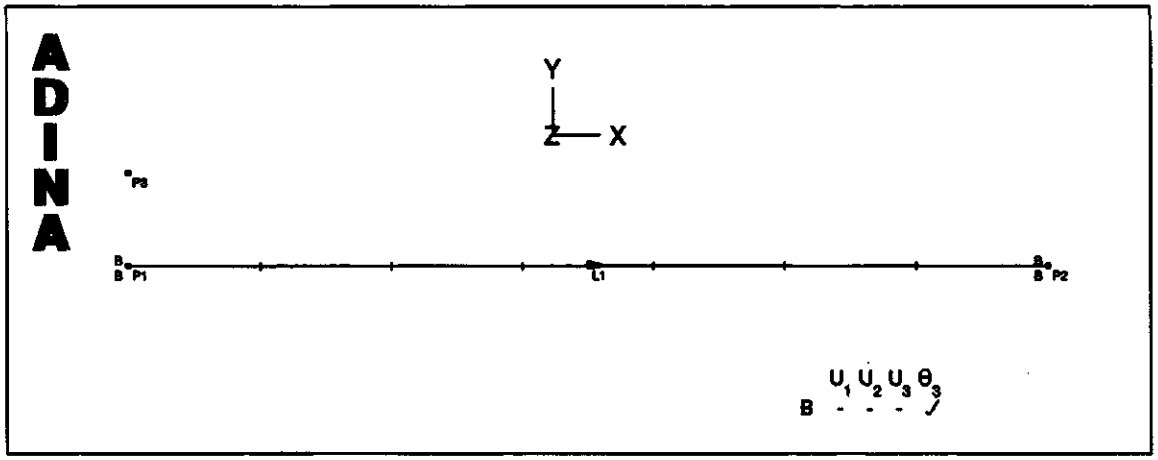

Figure A.5: Dividing the Beam into 7 Subdivisions.

ADINA generates a report in ADINA-PLOT about the number of nodes created, the element groups used and the number of elements created. The report appears in ADINA-PLOT as follows:

ADINA: AUI version 8.0.2, 23 February 2004:

simply supported Licensed from ADINA R&D, Inc.

Information for ADINA finite element model:

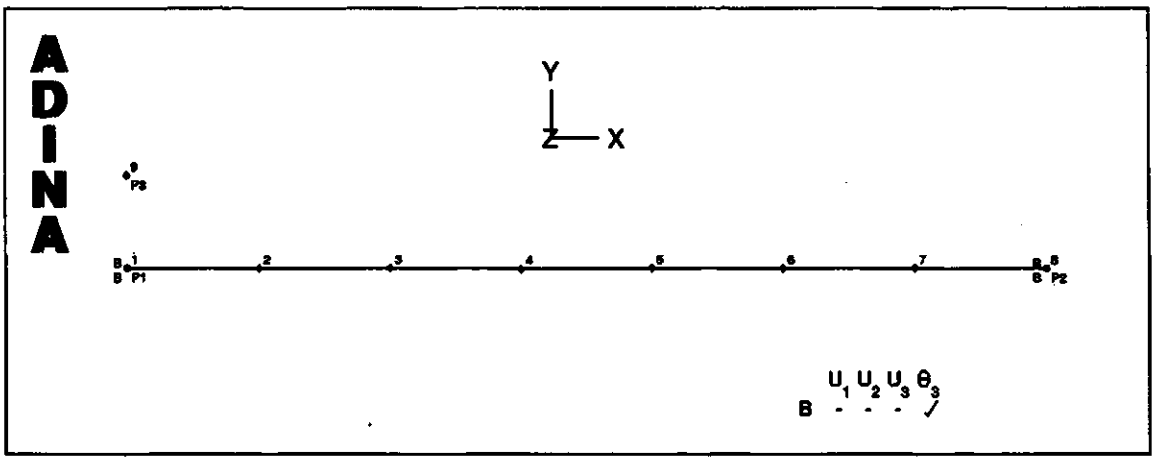

Figure A.6: Nodes for the 7 Subdivision Mesh of the Beam.

9 nodes.

1 element group:

Element group 1: 7 Hermitian beam elements.

7 elements total.

**** End of list.*

Analytically, the first three natural frequencies [31] were

$f_1 = 27.1$ Hz,

$f_2 = 108.4$ Hz,

$f_3 = 243.8$ Hz.

Frequency analysis via ADINA is performed to calculate the beam's first three natural frequencies and compare them to the analytical ones. For the model defined

above, with 7 subdivisions, the first three natural frequencies were as follows:

$f_1 = 27.0707$ Hz,

$f_2 = 108.287$ Hz,

$f_3 = 209.877$ Hz.

Comparing the analytical and numerical results for 7 subdivisions, it can be seen that the first two numerical natural frequencies were the same as the first two analytical ones while the third numerical natural frequency was far from its analytical one. This implied, that a finer mesh has to be used. Figure A.7 shows the beam divided into 8 subdivisions, and Figure A.8 shows the created nodes for 8 subdivisions.

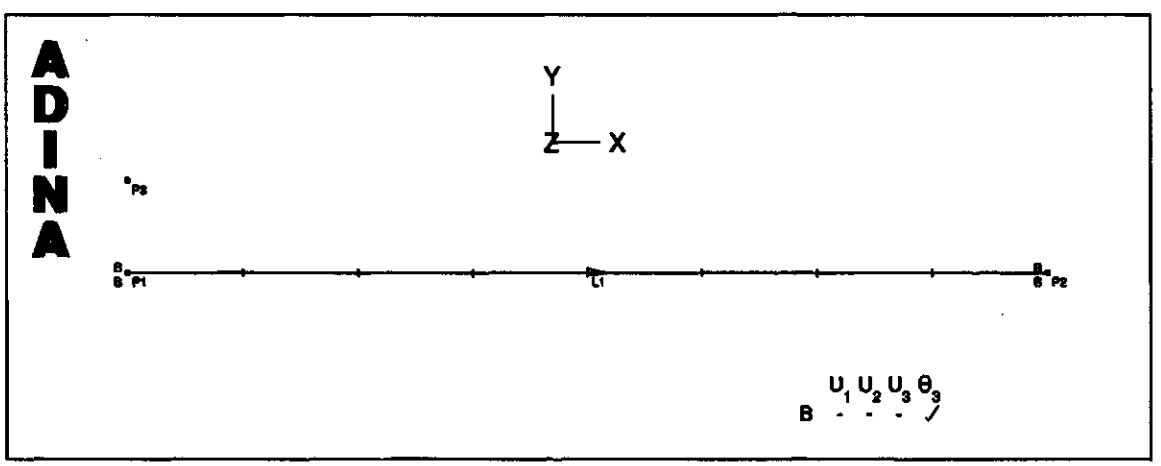

Figure A.7: Eight Subdivisions for the Simply Supported Beam.

The ADINA report for the 8 subdivision model was as follows:

ADINA: AUI version 8.0.2, 23 February 2004:

simply supported Licensed from ADINA R&D, Inc.

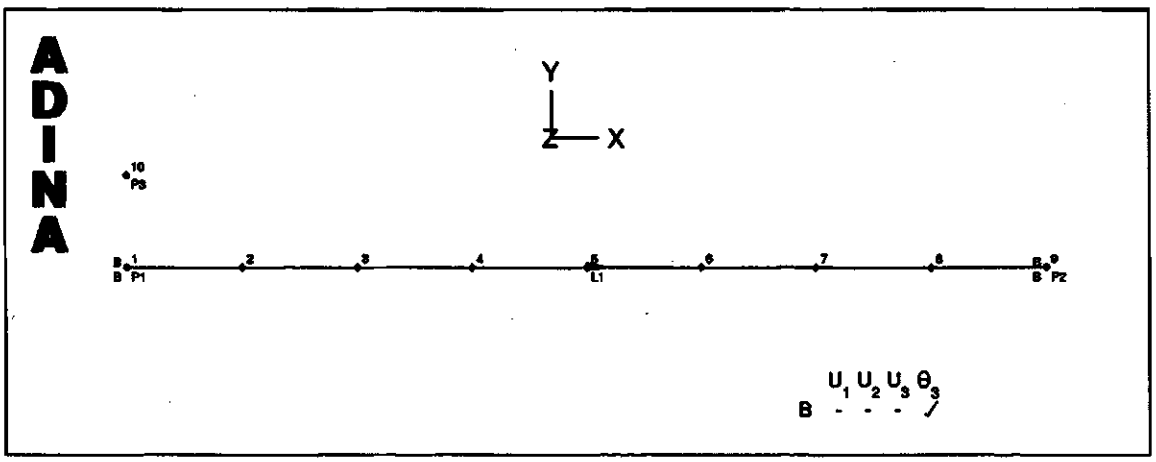

Figure A.8: Created Nodes for Eight Subdivisions Applied to the Simply Supported Beam.

Information for ADINA finite element model:

10 nodes.

1 element group:

Element group 1: 8 Hermitian beam elements.

8 elements total.

**** End of list.*

Performing the frequency analysis on the 8 subdivision as before, the following natural frequencies are obtained,

$f_1 = 27.0704$ Hz,

$f_2 = 108.268$ Hz,

$f_3 = 239.610$ Hz.

Table A.1 compares the analytical and numerical results for 8 subdivisions. The first and second natural frequencies have a percentage difference from the analytical of about 0.1 %, while the third natural frequency had an error from the analytical of less than 2 %.

Table A.1: Comparison Between Analytical and Numerical Results For 8 Subdivisions.

	First Natural Frequency (Hz)	Second Natural Frequency (Hz)	Third Natural Frequency (Hz)
Analytical	27.1	108.4	243.8
Numerical	27.0704	108.268	239.610
Percentage Difference	0.1 %	0.1 %	1.7 %

As increasing the number of nodes and elements gave better results, further refinement was done on the beam model. The beam was divided into 10 subdivisions. Figure A.9 shows the beam divided into 10 subdivisions, and Figure A.10 shows the nodes created for 10 subdivisions.

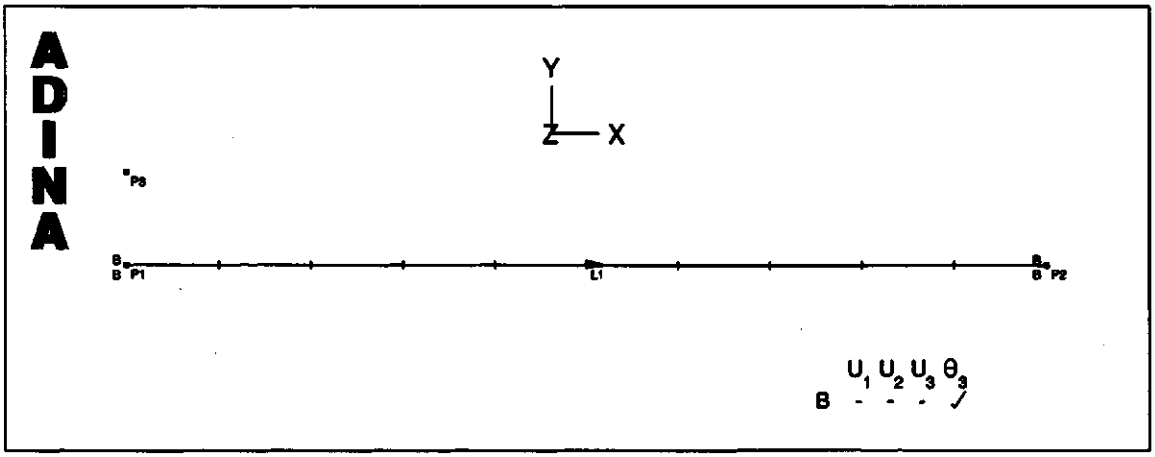

Figure A.9: Ten Subdivisions for the Simply Supported Beam.

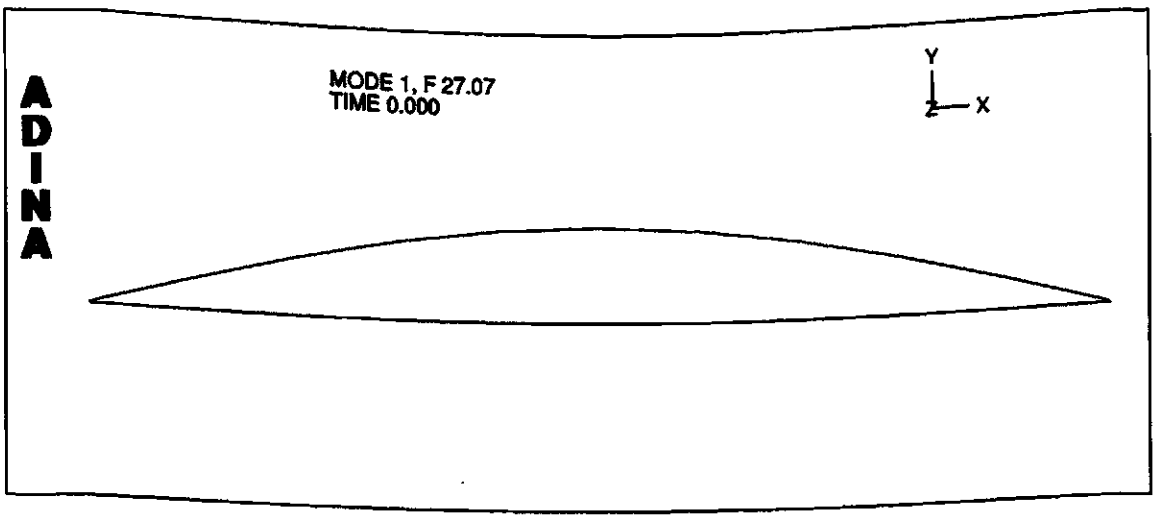

Figure A.11: First Mode Shape of a Simply Supported Beam.

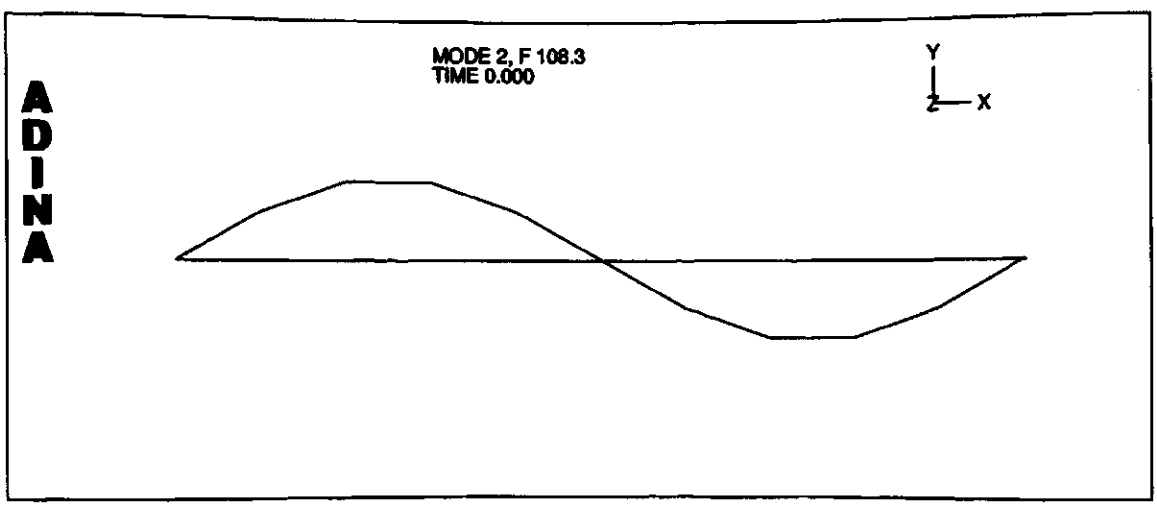

Figure A.12: Second Mode Shape of a Simply Supported Beam.

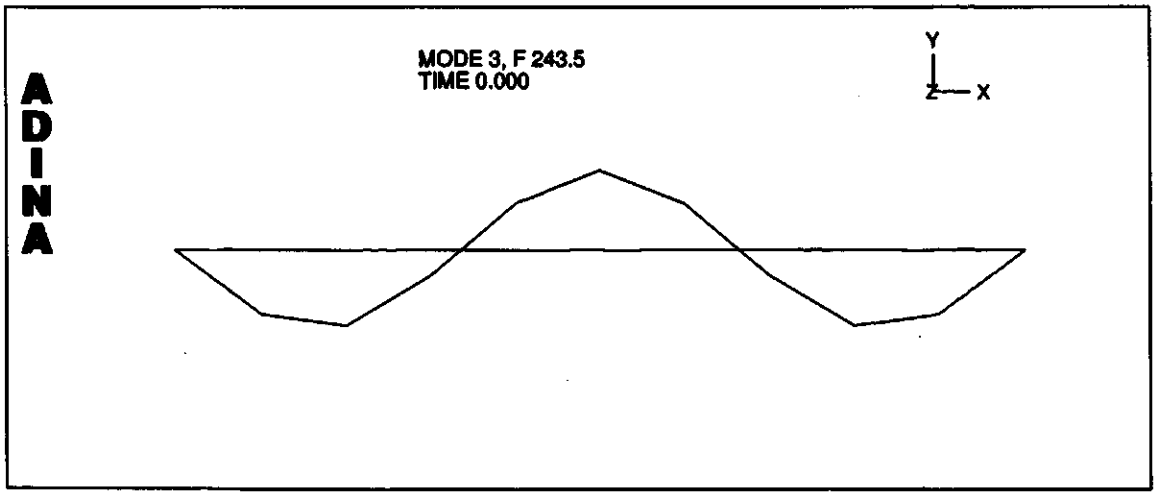

Figure A.13: Third Mode Shape of a Simply Supported Beam.